An Electronically-switched Sensor Array for Microwave Imaging

AN ELECTRONICALLY-SWITCHED SENSOR ARRAY FOR MICROWAVE IMAGING

By

ALEXANDER SAMUEL BEAVERSTONE, B.ENG.

A Thesis Submitted to the School of Graduate Studies in Partial Fulfillment of the Requirements for the Degree Master of Applied Science

McMaster University

MASTER OF APPLIED SCIENCE (2015)	McMaster University
(Electrical and Computer Engineering)	Hamilton, Ontario

TITLE: **An Electronically-switched Sensor Array for Microwave Imaging**

AUTHOR: Alexander Samuel Beaverstone
B.Eng. (Electrical Engineering)
McMaster University, Hamilton, Canada

SUPERVISOR: Natalia K. Nikolova, Professor,
Department of Electrical and Computer Engineering
McMaster University
Ph.D. (University of Electro-Communication)
Fellow, IEEE
P.Eng. (Ontario)
Canada Research Chair in High Frequency Electromagnetics

NUMBER OF PAGES: CXIII, 113

ABSTRACT

An array of electronically-switched circular patch antennas is designed for breast tissue imaging for the purposes of cancer screening. Each array element is connected to a dedicated heterodyne radio, which performs amplification and downconversion to a single, low intermediate frequency for improved signal recovery. Data acquisition is accomplished with a VNA-based architecture. Details of the design are provided and are accompanied by simulated and experimental data. A receiver sensitivity of at least -120 dBm is expected, and an imaging sensor switching dynamic range between ON and OFF states of at least 127 dB is demonstrated based on experimental measurements.

ACKNOWLEDGEMENTS

I would like to show my gratitude to my family – my mother Barbara and father Philip – for their encouragement and continued support in my pursuit of higher education. It was their careful investment of time and dedication to my upbringing that inspired me to consider a career in engineering, and their financial support that enabled me to achieve my goals. I would not have come this far were it not for their concern and their love.

I wish to thank my supervisor, Dr. Natalia K. Nikolova, for her wisdom and confidence, which prompted me to enroll in graduate studies and enrich my understanding of electromagnetism. Under her guidance, I have enjoyed the privilege of experiencing research work in a fascinating and compelling field of science, which has opened a new domain of possibilities I hope to discover.

Furthermore, my colleagues in the Computational Electromagnetics Research Laboratory at McMaster have provided me invaluable feedback on presentations and offered helpful suggestions in my research. In no particular order, I am grateful to have worked with Justin McCombe, Sheng Tu, Denys Shumakov, Jeff Thompson, Daniel Tajik, and Kaveh Moussakhani.

Finally, I'd like to thank Brandon, for his loving encouragement and kindness. His support has motivated me to continue with my research, and I am deeply touched by his interest in my work. His care has been invaluable to me.

CONTENTS

CHAPTER 1 INTRODUCTION

CHAPTER 2 IMAGING SYSTEM PERFORMANCE PARAMETERS

CHAPTER 3 PROPOSED SYSTEM ARCHITECTURE

CHAPTER 4 ANTENNA DESIGN

CHAPTER 5 RADIO RECEIVER FRONT-END DESIGN

CHAPTER 6 EXPERIMENTAL VERIFICATION

CHAPTER 7 CONCLUSION AND FUTURE WORK

LIST OF FIGURES

CHAPTER 1

INTRODUCTION

1.1. Background: Microwave Imaging

Microwaves occupy a significant portion of the electromagnetic spectrum used in the acquisition of images [1]. Their propagation characteristics make them an attractive candidate for a variety of applications. For example, in non-destructive testing (NDT), objects under test can be examined without disassembly by irradiating them with microwaves in order to characterize their material properties and to detect cracks in manufactured structures [2].

Microwave imaging has also been applied within medicine. Techniques used to produce images of biological specimens with microwave radiation have been investigated since at least as early as the 1970s; Larsen and Jacobi used modulated microwaves to irradiate canine kidneys, measuring the scattered radiation in order to reconstruct an image [3]-[5]. These early experiments demonstrated to the scientific community the viability of employing microwaves to generate images of tissues. Measurements of microwave propagation through tissues can elucidate material properties that may not be visible in other imaging modalities. For instance, the dielectric permittivity and the conductivity of tissues may be calculated in discrete regions using suitable reconstruction algorithms on acquired data [5]-[8]. Using this information, certain inferences may be made regarding the biological properties of this tissue, such as oxygenation levels, blood perfusion, and the concentration of substances in bodily fluids [1].

1.2. Motivation: Microwaves and Cancer

One of the most compelling and heavily investigated areas of research involving microwave imaging is the detection of cancer in tissues. Breast cancer imaging has received particularly strong attention in the research community for a variety of reasons, including the desire to abandon the use of ionizing x-radiation and the generally uncomfortable, often painful, mechanical compression of tissues during the regular cancer screening process [1].

In an effort to mitigate the discomfort associated with conventional mammography, some imaging systems have been constructed using cylindrical and hemi-spherical acquisition surfaces, in which the breast may rest pendant, hanging in a volume of space for measurement [9]-[12]. These systems may employ liquids of specific dielectric permittivity in order to more effectively couple the examined tissues electrically to the transmitting and receiving antennas [9][12], referred to in this thesis as liquid coupling media. This is done to minimize reflection losses due to the impedance mismatch between differing dielectric media (e.g. antenna materials, air, and tissue of examined patient).

With each medical microwave imaging system currently explored in the literature, however, there are common performance drawbacks that diminish image quality. These drawbacks include the mechanical uncertainty in the imaging probe system, and poor signal-to-noise ratio (SNR) due to the immense attenuation of signal in tissues. Furthermore, when extremely broadband equipment, such as commercially available vector network analyzers (VNAs) and broadband coaxial switches, are used in the imaging system, the dynamic range in the received signal can be negatively affected. This is due to the compromises made when designing the broadband componentry, as is commonly found in the commercial VNAs and microwave switches. It is advantageous, therefore, to avoid using this hardware when possible, by designing and optimizing similar custom equipment for a more limited bandwidth of frequencies.

An imaging system for breast cancer detection can better serve the large patient roster by being made small and inexpensive, so that deployment in a general practitioner’s office is possible. This can be done with modern microwave equipment, since printed circuit board transmission lines and surface-mount technology are both available for use in the frequencies typically explored in the literature, between 2 and 8 GHz [1][13][14]. Using modest breast compression without the inclusion of liquid coupling media, the doctor can perform an examination and avoid the complications of purchasing sterile chemicals and applying them to each patient, thereby facilitating quicker measurements and inter-examination clean-up. With compression of the tissues, the total path length from the microwave illuminating structure to the detection sensors is decreased, which benefits the system SNR with increased imaging signal power at each sensing element.

Finally, it is worthwhile pursuing the design of an imaging system that uses switched sensors. This reduces mechanical scanning, minimizing the mechanical positioning uncertainties, and reduces the total imaging time. Both effects can have a dramatic impact on the image quality, since positioning uncertainties can lead to artefacts [1][15] while long imaging intervals can lead to patient discomfort, increased likelihood of patient/imaging volume motion (highly deleterious to image quality), and increased likelihood of artefact due to the temperature-dependent electrical parameters of the tissue, which are precisely the source of image contrast [1][2][16]. Various switched sensor arrays have been implemented in which the sensor signals are consolidated on a single output port [17]. The modulated scatterer technique [18] offers the further advantage of reducing the total imaging system channel count for ease of integration with high-performance microwave equipment, such as vector network analyzers, which have only a limited number of ports available.

1.3. Contributions: Biomedical Microwave Imaging

The author’s contributions to the field of biomedical microwave imaging include the following.

1) The design of a compact patch antenna element on high permittivity substrate for planar scanning of breast tissues, reported in [19].
2) The design of an electronically-switched sensor array with dual polarization capability and an integrated downconversion stage for the efficient transmission of imaging data [19][20].
3) The design of a custom vector data acquisition architecture suitable for use in microwave imaging using commercially available components.

1.4. Thesis Outline

This thesis is divided into 7 chapters:

Chapter 2 describes the parameters used to evaluate the performance of a biomedical microwave imaging system. Technical challenges affecting image quality are listed, followed by descriptions of various figures-of-merit used to quantify an acquisition system’s ability to overcome these challenges.

Chapter 3 outlines the proposed imaging system architecture explored in the remaining chapters of this thesis. It begins with a brief introduction to the techniques used in microwave imaging, and then continues with an elaboration on the design of an imaging system architecture, chosen to overcome the limitations of previously reported systems.

Chapter 4 begins the full system design by describing the antenna choice for the microwave imaging sensor. It begins with a summary of the requirements for the design of the antenna, referencing the performance goals outlined in Chapter 3. Next, a set of specifications is given, from which an initial design is selected for optimization. Performance measurements from simulation and experimental implementation are given as justification of the final design choice.

Chapter 5 describes the electronic components that follow in the signal path of the proposed measurement instrument. Amplifiers and frequency translation devices are chosen for use in a set of discrete radio front-end modules, each of which are coupled to the imaging sensors used in the complete system.

Chapter 6 follows with the construction of a prototype imaging sensor, which is evaluated both in simulation and in experimental measurements using real imaging phantoms in a raster scanning mechanism. Results are presented as verification of the design.

Chapter 7 completes the thesis with a conclusion and summary of suggested future work.

A full bibliography is given at the end.

REFERENCES

[1] N.K. Nikolova, “Microwave biomedical imaging,” *Wiley Encyclopedia of Electrical and Electronics Engineering*, pp. 1–22. (published on-line Apr. 25, 2014).

[2] M. Pastorino, *Microwave Imaging*. Hoboken, NJ: John Wiley & Sons Inc., 2010.

[3] L.E. Larsen and J.H. Jacobi, eds., *Medical Applications of Microwave Imaging*. New York: IEEE Press, 1986.

[4] L.E. Larsen and J.H. Jacobi, “Microwave interrogation of dielectric targets. Part I: By scattering parameters,” *Med. Phys.*, vol. 5, no. 6, 1978, pp. 500–508.

[5] L.E. Larsen and J.H. Jacobi, “Microwave interrogation of dielectric targets. Part II: By microwave time delay spectroscopy,” *Med. Phys.*, vol. 5, no. 6, 1978, pp. 509–513.

[6] R.K. Amineh, M. Ravan, A. Trehan, and N.K. Nikolova, “Near-field microwave imaging based on aperture raster scanning with TEM horn antennas,” *IEEE Trans. Antennas Propagat.*, vol. 59, no. 3, pp. 928–940, Mar. 2011.

[7] J.R. Thompson, J.J. McCombe, S. Tu, and N.K. Nikolova, “Quantitative imaging of dielectric objects based on holographic reconstruction,” 2015 *IEEE Int. Radar Conf.*, Arlington, VA.

[8] S. Tu, J.J. McCombe, D.S. Shumakov, and N.K. Nikolova. “Fast quantitative microwave imaging with resolvent kernel extracted from measurements,” *Inverse Problems,* vol. 31, no. 4, 2015, 045007.

[9] M. Klemm, J.A. Leendertz, D. Gibbins, I.J. Craddock, A. Preece, and R. Benjamin, “Microwave radar-based differential breast cancer imaging: imaging in homogeneous breast phantoms and low contrast scenarios,” *IEEE Trans. Antennas Propagat.,* vol. 58, no. 7, pp. 2337–2344, Jul. 2010.

[10] P.M. Meaney, M.W. Fanning, D. Li, S.P. Poplack, and K.D. Paulsen, "A clinical prototype for active microwave imaging of the breast," *IEEE Trans. Microwave Theory and Techniques*, vol. 48, no. 11, pp. 1841−1853, Nov. 2000.

[11] J. Bourqui, J. M. Sill, and E. C. Fear, "A prototype system for measuring microwave frequency reflections from the breast," *Int. Journal of Biomedical Imaging*, vol. 2012, Article ID 851234, 12 pages, 2012.

[12] M.E. Bialkowski, A.M. Abbosh, Y. Wang, D. Ireland, A.A. Bakar, and B.J. Mohammed, "Microwave imaging systems employing cylindrical, hemispherical and planar arrays of ultrawideband antennas," *Microwave Conf. Proc. (APMC), 2011 Asia-Pacific*, pp. 191−194, Dec. 2011.

[13] J.C. Lin, "Frequency optimization for microwave imaging of biological tissues," *IEEE Proc.*, vol. 73, no. 2, pp. 374–375, Feb. 1985.

[14] D.M. Pozar, *Microwave Engineering*. 4th ed., Hoboken: John Wiley & Sons, Inc., 2012.

[15] T.S. Curry, J.E. Dowdey, and R.C. Murry, *Christensen's Physics of Diagnostic Radiology*. 4th ed., Philadelphia: Lippincott Williams & Wilkins, 1990.

[16] D. Faktorová, "Temperature dependence of biological tissues complex permittivity at microwave frequencies," *Adv. in Electrical and Electronic Eng.*, vol. 7, pp. 354−357, 2008.

[17] J.-C. Bolomey, “Technology-based analysis of probe array systems for rapid near-field imagery and dosimetry,” *2014 8th European Conf. Antennas and Propagat. (EuCAP)*, pp. 3115−3119, April 2014.

[18] J.-C. Bolomey and F.E. Gardiol, *Engineering Applications of the Modulated Scatterer Technique*. Norwood, MA: Artech, 2001.

[19] A.S. Beaverstone and N.K. Nikolova, “Switched sensor array for near-field microwave imaging of tissue,” *IEEE Int. Symp. Antennas Propagat. North American Radio Science Meeting*, no. 4765, Jul. 2015.

[20] A.S. Beaverstone and N.K. Nikolova, “Modeling and design of a switched transceiver array for tissue imaging,” *IEEE MTT-S Int. Conf. Num. EM and Multiphys. Modeling and Opt. 2015*, Aug. 2015.

CHAPTER 2

IMAGING SYSTEM PERFORMANCE PARAMETERS

2.1. Background: Technical Challenges in Microwave Imaging

Every microwave imaging system has advantages and disadvantages, which may justify the large variety of system designs explored in the research literature. Some of the most significant problems with image fidelity come as a result of mechanical positioning uncertainties in the imaging system itself. Depending on the size of the acquisition surface, the dimensions of each imaging sensor, and the type of scanning employed, positioning errors accumulate in the data, leading to erroneous measurements. Further, depending on the nature of the acquisition surface, whether or not it places the imaged volume in a mechanically fixed position, patient motion in clinical trials of these imaging systems is a source of significant error in the acquired data [1].

In addition to these issues, the electrical interconnects and circuit layout have a decidedly large impact on the signal fidelity as it enters the acquisition surface and is eventually transmitted to the image processing computer. Cables used to connect imaging sensors to system modules induce stochastic errors when their motion is enabled by vibrations during the positioning of either the imaging probe or the imaged volume. It is observed that, particularly at high frequencies in the microwave domain, cable motion can lead to varying insertion loss and phase delay, thereby corrupting incoming imaging information to be retrieved by the system during a measurement [2]. Interconnections between elements of the imaging system also lead to diminished performance as these connections can disturb impedance matching, causing reflection and subsequent loss of signal strength.

Matching the sensors to the imaged volume in terms of their impedance is crucial so that as little of the imaging signal will be lost to reflection and refraction. This is done by assuming a choice of permittivity and conductivity that best represents the same, averaged material parameters in human breast tissues for a desired frequency range [3]. By selecting a single permittivity to represent tissues in the measurement frequency range, antennas can be fabricated in a medium with the same electrical characteristics so that the insertion loss between antennas across a volume segment is minimized.

The complexity of biomedical imaging with microwaves becomes quickly apparent when one recognizes the number of measurements necessary to construct a meaningful image of a tissue volume. Unlike the typical measurements made at high frequencies on single to quadruple port devices, an imaging system must make hundreds or even thousands of such measurements over many points in space so that sufficient information is collected about the subject for image reconstruction. This complexity not only slows data collection, but also slows the reconstruction process, as these data must be subsequently processed by an algorithm, often featuring math operations that have high computational costs, such as least squares fitting and matrix manipulations [4]. Any method of reducing the total time required to produce an image is valuable when tissue diagnosis is needed. Quick data acquisition is critical when an imaging modality is considered for implementation in a real cancer screening environment.

It is demonstrated in [5] that there is temperature dependence in the electrical properties of tissue. As such, prolonging the time of an image acquisition may lead to erroneous conclusions regarding the data collected in a medical examination scenario, since the dielectric properties of tissue are dynamic, and therefore present time-varying signals to the acquisition system. If an acquisition is performed on an in-vivo specimen that has dense fibroglandular tissues surrounding an embedded tumor, changes in blood concentration and other biological parameters may distort or obscure the visibility of the cancerous growth. Moreover, even the imaging phantoms used to calibrate the system are subject to time-variance in their dielectric properties, since they undergo chemical changes with respect to temperature [3]. It is best, therefore, to design a system that minimizes the acquisition time in order that these sources of random error affects only minimal impact on the measurements.

Regardless of the geometry of the desired acquisition surface, every microwave imaging modality suffers in performance if the system has poor signal-to-noise ratio (SNR) and small dynamic range. Maximizing these figures-of-merit is crucial in obtaining high-quality, meaningful images. They determine the limits of available contrast and uncertainty in the system, regardless of the acquisition surface, frequencies, and reconstruction algorithm used.

2.2. Evaluation of the System Performance

The performance of an imaging system may be characterized in a diagnostic scenario using the statistical measures of sensitivity and specificity [6]. However, in an engineering context, it is more valuable instead to consider the performance measurements of the system's components, such as return loss, insertion loss, compression and noise figure, as these enable an engineer to make informed decisions regarding the hardware choices made in the final design. Good choices at an early stage ensure high fidelity of the imaging signal.

Noise, as an electromagnetic phenomenon, is a stochastic process that can diminish the sensitivity of an imaging system. Image information can become embedded in noise if the imaging signal is sufficiently weak with respect to the noise power. It is therefore critical that the imaging system design incorporate low-noise components, allowing for higher sensitivity in tissue imaging scenarios, where signal attenuation is great. The *noise figure* of a component can be used to quantify the system's sensitivity, which will determine the system's SNR.

When making quantitative measurements of tissue properties, such as conductivity and permittivity, information can be obscured due to nonlinearites in the instrumentation. For instance, if the received imaging signal in a receiver is high enough in power that it causes saturation of internal amplifiers in the signal chain, the imaging system may then misrepresent the true magnitude of the tissue parameter of interest. When calibration is not possible to correct for this, the result is that artefacts can appear in the data, leading to possible false positives or false negatives in the diagnosis of malignant tissues. Thus, it is important to quantify the maximum received signal strength before nonlinear effects, such as signal compression, occur. The *1-dB compression point* is defined as the power level at which the gain through a network decreases by 1 dB from its small-signal value [7]. It is measured after the design of the imaging system signal path to determine the maximum power acceptable at the imaging receiver antenna terminals before signal distortion occurs.

Combining the noise floor with the saturation point of the instrumentation, one may obtain a useful measure of system *dynamic range*, which dictates the necessary illumination power of the system for a given thickness of imaged volume. This information further determines the clinical viability of a system by implying how much absorbed radiation dose will be incurred in a real patient diagnostic scenario. Provided that the sensitivity of the system is sufficient, only modest transmitter power will be necessary, thereby ensuring that the imaging system complies with the government-regulated specific absorption rate limits on radiation exposure.

2.3. Conclusions

Technical challenges faced by researchers in the construction of successful microwave imaging systems are presented as context for the continued development of novel architectures. Several figures-of-merit are presented for consideration in the evaluation of an imaging system design.

REFERENCES

[1] T.S. Curry, J.E. Dowdey, and R.C. Murry, *Christensen's Physics of Diagnostic Radiology.* 4th ed., Philadelphia: Lippincott Williams & Wilkins, 1990.

[2] A. Hati, C.W. Nelson, D.A. Howe, N. Ashby, J. Taylor, K.M. Hudek, C. Hay, D. Seidef, and D. Eliyahu, “Vibration sensitivity of microwave components,” *2007 Joint 21st European Freq. Time Frm. IEEE Int. Freq. Control Symp.*, pp. 541–546, May 29–June 1, 2007.

[3] Y. Baskharoun, A. Trehan, N.K. Nikolova, and M.D. Noseworthy, “Physical phantoms for microwave imaging of the breast,” *2012 IEEE Topical Conf. Biomedical Wireless Technologies, Networks, and Sensing Systems (BioWireleSS)*, pp. 73–76, Jan. 15–18 2012.

[4] T. Gunnarsson, “Microwave imaging of biological tissues: applied toward breast tumor detection,” Licentiate thesis, Dept. of Comp. Sci. and Electronics, Mälardalen Univ., Västerås, Sweden, 2007.

[5] D. Faktorová, “Temperature dependence of biological tissues complex permittivity at microwave frequencies,” *Adv. in Electrical and Electronic Eng.*, vol. 7, pp. 354–357, 2008.

[6] N.K. Nikolova, “Microwave biomedical imaging,” *Wiley Encyclopedia of Electrical and Electronics Engineering*, pp. 1–22. (published on-line Apr. 25, 2014).

[7] National Instruments, “1 dB gain compression measurement (P1dB)”, [Online]. Available: http://www.ni.com/white-paper/2952/en/

CHAPTER 3

PROPOSED SYSTEM ARCHITECTURE

3.1. Introduction

As mentioned in the previous chapters, a variety of microwave imaging systems have been explored in the literature. Within the currently investigated biomedical systems, several acquisition methods are used in breast cancer imaging. These methods can involve scanning on planar, cylindrical, and hemi-spherical surfaces, employing RF switching and mechanical translation of the imaging probe. Both cylindrical and hemi-spherical surfaces offer a means of acquiring data when the breast is more or less in its conventional state, unaffected by mechanical alteration, such as compression. In the interest of patient safety and cooperation, these systems might therefore be attractive to the imaging community. However, in planar acquisition surfaces, modest compression of the tissue can be exploited to enhance signal propagation and lessen the microwave path loss. Further, compression to one or more of a minimal set of standard thicknesses can enable more accurate image generation, since only a minimal set of measurement scenarios need be considered when designing imaging phantoms for system calibration. Thus, a design trade-off arises in patient comfort and image accuracy and measurement repeatability. Here, a solution is proposed to resolve some of the performance issues faced by pre-existing systems. In view of the significance of maximizing the imaging system SNR, a planar, electronically switched sensor array with organ compression is explored in this thesis.

3.2. Principles of Microwave Imaging

There are numerous techniques available for the generation of images from raw measurement data using microwaves. In imaging, the type of data collected and the mechanism with which it is acquired both have a decisive impact on the nature of the information embedded in the images. Using the holography approach described in [1], the data type used is a set of *S*-parameters, measuring the transmission and reflection of incident microwave radiation on an imaged target. The *S*-parameters are measured within a fixed band of frequencies by translating transmitting and receiving antennas in a raster scan fashion around an imaged target, coupling energy into and out of the target over a planar surface with uniform spatial sampling, as is illustrated in FIG. 3-1:

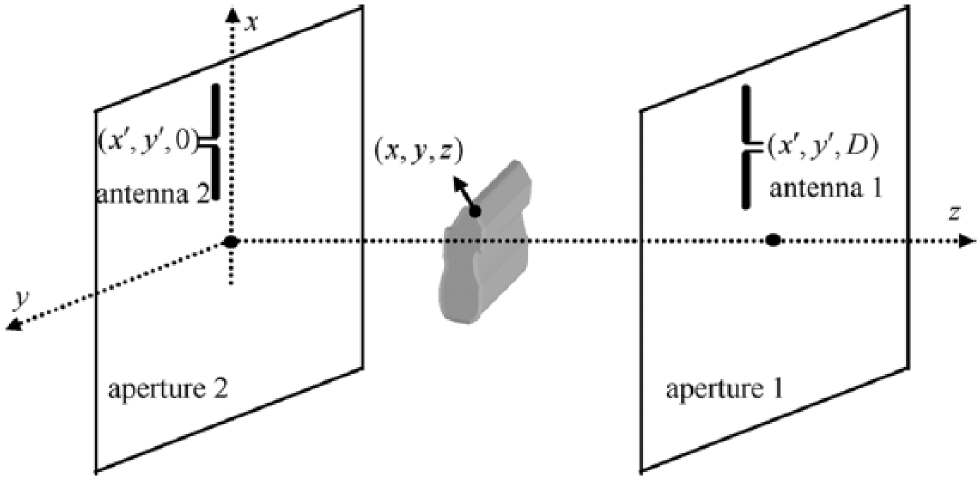

FIG. 3-1. 3D Microwave holography setup [1].

It is demonstrated in [1] that the *S*-parameter data represents the electric field at a specific measurement point in space. By using this model, one may extract an image of a target simply by acquiring complex-valued *S*-parameters at discrete locations in space for a desired band of frequencies, then feeding the data into an appropriate algorithm for image reconstruction. This enables one to use a vector network analyzer (VNA), which is capable of being calibrated with high-precision impedance standards, and therefore can have considerable dynamic range and low noise floor, especially when applying averages to collections of repeated measurements [2]. These *S*-parameter data have the further advantage of offering flexibility in computer analysis, since many RF and microwave software suites operate on these data directly. The incorporation of experimental *S*-parameter data in microwave design and simulator environments allows for improved tuning and optimization of hardware structures, so that their performance better represents the scenario of measurement with imperfect, manufactured materials.

FIG. 3-2 shows a diagram of a typical VNA architecture, for the acquisition of test signals used to derive S-parameters.

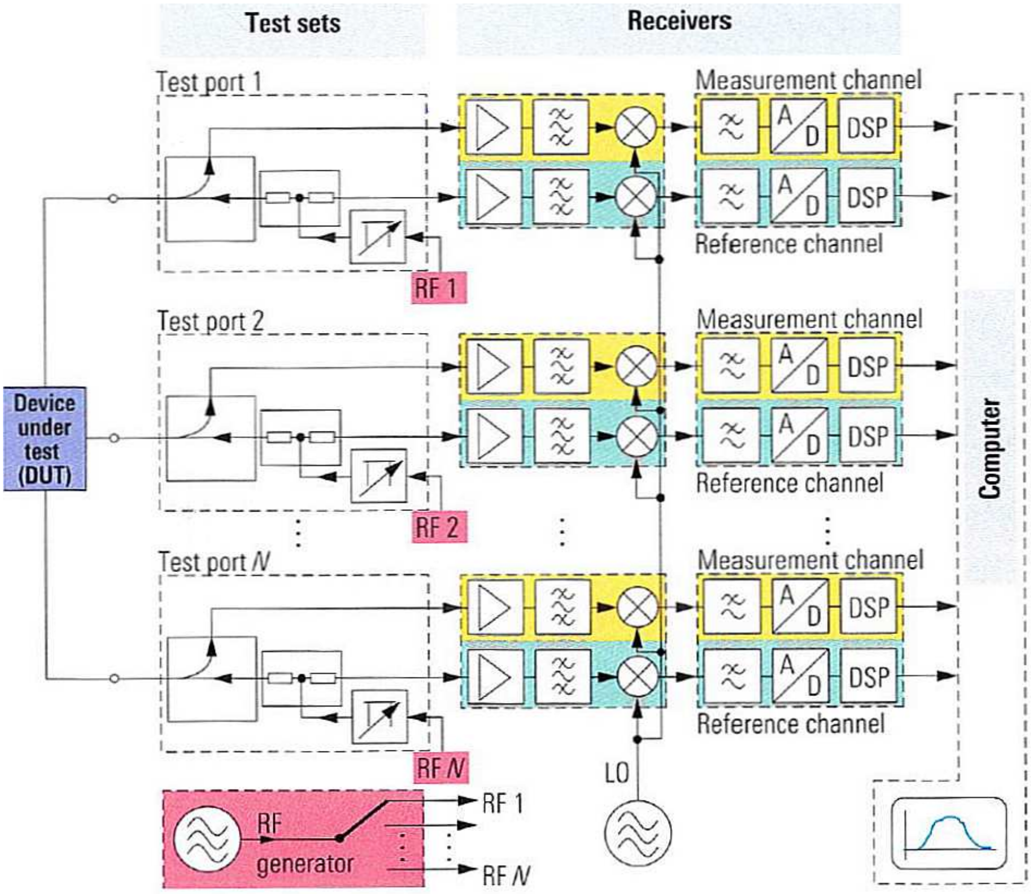

FIG. 3-2. Block diagram of a standard *N*-port vector network analyzer [3].

Many designers of RF and microwave equipment implement a variation of this schematic, including additional frequency translation modules, power levelling, and signal digitization, depending on the frequencies and signal powers used in the measurement. Often, these instruments are designed to operate over an extremely wide bandwidth of frequencies, extending from as low as several kilohertz to as high as the terahertz range [4]. Operating on enormous bandwidths is often necessary when the VNA is used to characterize electronic devices across multiple bands of operation, such as amplifiers and filters. In the case of tissue imaging, however, trade-offs in microwave propagation loss and image resolution are made so that it is sufficient to constrain the bandwidth to a far more limited region of the electromagnetic spectrum, as is explained in more detail in Chapter 4. It is, therefore, desirable to construct a VNA using components designed specifically for the band of interest. These components can provide superior performance because they can be optimized more aggressively for lower noise figure, insertion loss, and return loss in a specific band as compared with the extremely wideband variants, where compromises must be made to achieve uniformity across all frequencies.

Frequency translation is of particular importance in the design of signal analysis equipment, like network analyzers. The heterodyne technique is regularly exploited to achieve high performance in radio receivers by translating a desired signal to one or more intermediate frequencies (IF) [5]. Each IF is processed individually by an amplify-and-filter stage, removing artifact signals such as aliases, spurs, harmonics, and images. Further, a sufficiently low IF can be chosen in the final conversion stage, allowing a designer to use very sensitive detectors and digital signal processing devices, since high selectivity filters and high dynamic range detectors are more available at low frequencies.

3.3. Design Proposal

This thesis describes the design and evaluation of an electronically switched sensor array for microwave imaging, with focus on medical applications in breast cancer screening. The system description includes the transmitting and receiving antenna structures (elaborated in Chapter 4) and a data acquisition architecture used for signal detection and processing. In this section, the proposed architecture is described in 3 parts: a high-level schematic is given, illustrating the principle benefits of such a system; a low-level schematic is shown, describing the signal path and the components necessary to achieve the expected performance; and finally, a sensor-level diagram is shown, highlighting the integrated front-end receiver module used to provide the imaging signal to the remaining signal processing sections of the system.

As described in the Motivation section of the first chapter (Section 1.2), the proposed imaging system should: 1) attempt to mitigate mechanical positioning errors, 2) incorporate components optimized for use in the frequencies of interest, 3) achieve good impedance matching between the scanning system antennas and the imaged volume, and 4) acquire imaging data quickly. All four design goals are achievable with a switched sensor array, using conventional microwave techniques and components.

FIG. 3-3 shows the schematic for a microwave imaging system, based on a 2-port VNA architecture, and a bias-switched array of miniature radio receivers.

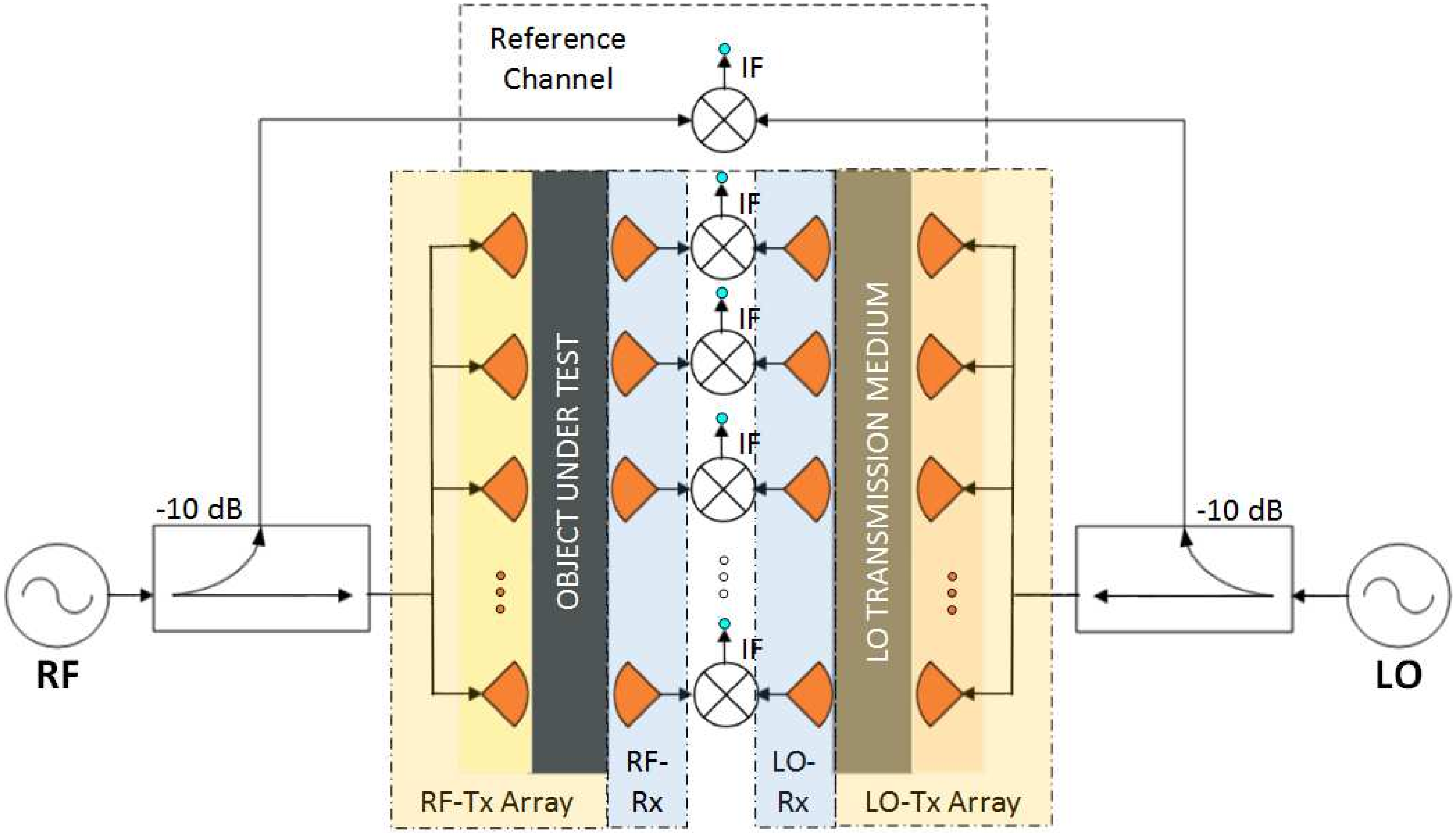

FIG. 3-3. High-level diagram of the proposed imaging system.

There are 5 primary components depicted in the previous figure:

1. Transmitting antennas (RF-Tx, LO-Tx):

   Identical to Rx antennas, oriented so that each Tx is directly opposite an Rx element, along boresight and in polarization match

2. Receiving antennas (RF-Rx, LO-Rx):

   Dual set of identical antennas, in mirror-symmetry, connected to receive microwave power through OUT and LO transmission medium

3. Frequency translation devices (mixers):

   Active mixers connected to both the RF-Rx and LO-Rx antenna arrays, used for downconversion of the RF signal to IF (or possibly baseband)

4. Oscillator sources (RF, LO):

   High-frequency sources used for illumination of OUT and LO transmission mediums

5. Directional couplers (-10 dB):

   Wideband couplers, used to derive low-power reference signals from both oscillator sources for generation of a reference signal at the system IF

This system interrogates an object under test (OUT) with two planar antenna arrays: one transmitting set (RF-Tx), and one receiving set (RF-Rx). Illumination of the OUT is performed with the RF-Tx antenna array, irradiating the OUT with microwave power generated by the RF oscillator (5 GHz $\leq f_{RF} \leq$ 8 GHz). One of the radio receivers in the RF-Rx array recovers the microwave power traveling through the OUT; this is the imaging signal. Notice that the Rx section contains mixers. These downconvert the received RF signal from the microwave spectrum (f_{RF}) to a much lower frequency, called the intermediate frequency (f_{IF}). Each mixer requires a local oscillator (LO) signal, generated by the LO source, which is in phase lock with the RF source, in order to downconvert the imaging signal to the system's intermediate frequency f_{IF}:

$$f_{IF} = f_{RF} - f_{LO} . \tag{3.1}$$

The novelty in this system is the wireless transmission of the LO signal through a LO transmission medium (see FIG. 3-3). This is enabled by the LO-Rx antenna array, which is a mirror image of the RF-Rx array. The LO power is transmitted wirelessly by an element of the LO-Tx array directly facing its LO-Rx counterpart, which is biased in the ON state.

The mixers used in this downconversion are active components. They have conversion gain, unlike their passive counterparts, and can be used as radio frequency switches by changing the biasing applied to them between ON and OFF states, as is demonstrated in Chapter 5. Thus, microwave power is coupled into the OUT through one pair of antennas at a time (RF-Tx and RF-Rx), switching between them electronically. Simultaneously, the LO power is coupled through the LO medium using the LO antenna pair on the opposite side of the Rx array (with LO-Rx and LO-Tx). Due to the antenna design constraints elaborated in Chapter 4, there is an appreciable spatial separation between adjacent antenna elements of the array (1.35 cm). In order to accomplish better spatial sampling than that of electronic scanning alone, additional mechanical translation should be employed. By replacing a full-scale *x*-*y* mechanical scan with a considerably smaller scanned area, it is possible to reduce the total acquisition time by orders of magnitude, while maintaining dense sampling. This is critical in a cancer screening scenario.

Notice that the diagram in FIG. 3-3 represents all antennas in the system with the same symbol. This is done not only as a convenience, but also to signify a benefit in adopting this architecture. In the proposed system, the intention is to use the same antenna design for all 4 arrays: RF-Tx, RF-Rx, LO-Tx, and LO-Rx. In the central Rx section, every array element is followed by a dedicated pair of low-noise amplifiers (LNAs), used to provide additional gain to the received signal before entry to the mixer, as is shown in the sensor-level diagram in FIG. 3-4. Notice that there are no LNAs connected in series with the LO antenna. The addition of LNAs in this signal path is not anticipated as necessary, as the LO transmission medium can be designed for low loss (small tanδ/thickness).

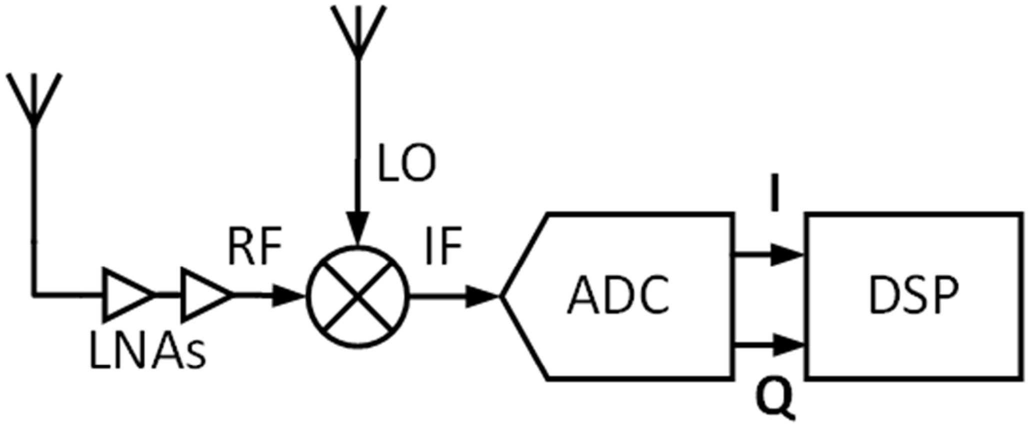

FIG. 3-4. Sensor-level diagram.

The downconverted imaging signal at f_{IF} is chosen to be sufficiently low in frequency (below 40 MHz) so that inexpensive transmission lines or power combiners can be used to consolidate all receiver array ports into a single output port. The downconverted signal is then subjected to signal processing. A low IF means less signal attenuation and distortion, and minimizes design complexity. This enables greater imaging system dynamic range. The consolidation of all receiver outputs into one port also facilitates the use of a single, inexpensive signal digitizer, operating close to baseband, which can be optimized separately from the RF front-end. An analog-to-digital converter can be chosen for operation at modest frequencies.

In FIG. 3-5, a low-level diagram is shown, describing the signal path in more detail.

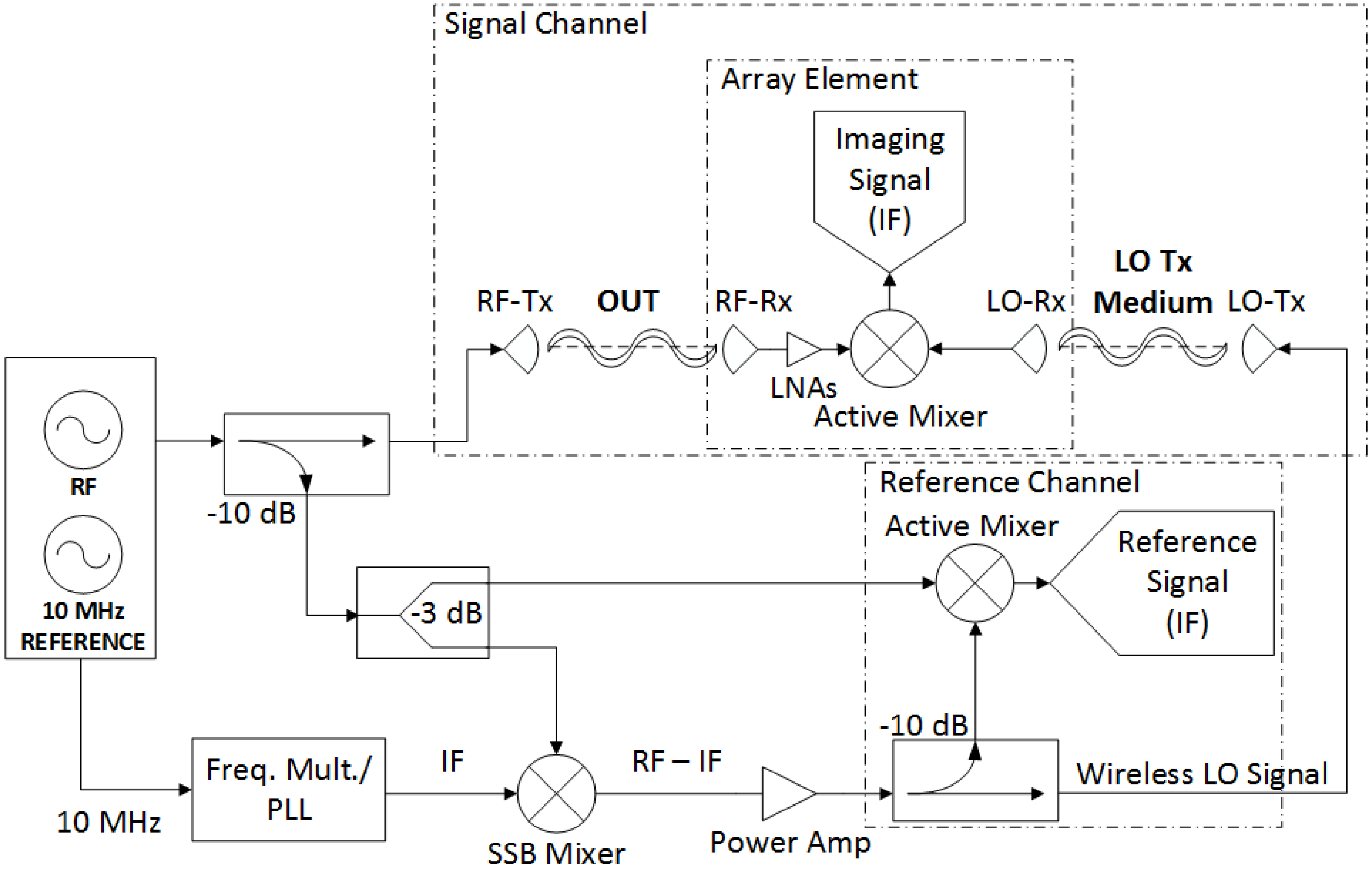

FIG. 3-5. Low-level diagram of imaging and reference channels in the proposed data acquisition system.

Notice that there is a block containing an RF oscillator and a 10 MHz reference. This block represents a continuous wave (CW) microwave source, consisting of an yttrium iron garnet (YIG) phase-locked oscillator and associated control circuitry. A YIG source is chosen for its excellent phase noise performance and spectral purity characteristics [6]. As the source produces a reference signal that is in phase lock with the RF output, this reference can be used to derive the LO signal, which is offset from the RF signal by the IF. The LO signal is produced first by translating the 10 MHz reference to the appropriate IF (chosen in Chapter 5 as 30 MHz for prototyping) using either a PLL or a frequency multiplier. This IF signal is then fed into a single sideband mixer, or Hartley mixer, which is capable of selectively translating an input signal to another band without introducing a strong image component in the spectrum [7]. This is in contrast to a conventional mixer, which takes its input RF and LO signals and combines them to form two components: $f_{LO}+f_{RF}$ and $f_{LO}-f_{RF}$. Here, the Hartley mixer takes the input (imaging system IF) and a sample of the RF signal (provided by a directional coupler and a 3-dB power splitter) and combines them to yield only one sideband: $f_{RF}-f_{IF}$. This signal is amplified and subsequently broadcast to the switched sensor array as the wireless LO signal.

In FIG. 3-5, an output is labeled as *Reference Signal (IF)*. This refers to the signal used in the system to generate the *S*-parameters for a given measurement, comparing the magnitude and phase of the received imaging signal with the reference channel. This reference channel the same active mixer used in the switched sensor array, and is derived from samples of the RF and LO signals directly.

When scanning an OUT, the output of the RF/LO source is controlled digitally by a computer, altering its frequency by increasing the value by a step dictated by the operator-controlled total number of desired frequency points. The frequency of the source is swept, making discrete frequency measurements at every coordinate position of the imaging probe.

The data are digitized by an analog-to-digital convertor (ADC). Magnitude and phase information may be recovered either by using I/Q mixers and sampling both channels for processing, or by implementing a phase detector and power sensor structure, as is described in [8][9]. The bit resolution of the ADC should be chosen to satisfy a minimum bound on the desired SNR of the radio receiver, according to the following formula [10]:

$$SNR = 6.02N + 1.76\,\mathrm{dB} \tag{3.2}$$

where N is the number of bits in the ADC output.

3.4. Conclusions

An imaging system design for biomedical applications is proposed for use in the ultrawideband spectrum. The described system reduces image artefact due to mechanical translation by minimizing the imaging probe motion necessary to achieve sufficient spatial sampling, using an electronically scanned array of sensors. This method also aims to reduce the time required to acquire imaging data and incorporates integrated radio receivers at each sensor, minimizing the risk of data loss due to the attenuation of the microwave signals through long transmission lines.

REFERENCES

[1] R. K. Amineh, M. Ravan, A. Khalatpour, and N.K. Nikolova, "Three-dimensional near-field microwave holography using reflected and transmitted signals," *IEEE Trans. Antennas Propagat.*, vol. 59, no. 12, pp. 4777–4789, Dec. 2011.

[2] Keysight Technologies, "Understanding and improving network analyzer dynamic range, application note," [Online]. Available: cp.literature.agilent.com/litweb/pdf/5980-2778EN.pdf

[3] M. Hiebel, *Fundamentals of Vector Analysis*. 1st ed., München: Rohde & Schwartz GmbH & Co. KG, 2007.

[4] Keysight Technologies PNA Network Analyzer, 300 kHz to 1.1 THz, http://www.keysight.com/en/pc-1000001745%3Aepsg%3Apgr/pna-network-analyzers-300-khz-to-11-thz?cc=CA&lc=eng

[5] National Instruments, "Super-heterodyne signal analyzers description and applications," [Online]. Available: http://download.ni.com/evaluation/rf/Super_Heterodyne_Signal_Analyzers.pdf

[6] A. Chenakin, “Select a VCO or YIG for a PLL synthesizer?” [Online]. Available: http://mwrf.com/active-components/select-vco-or-yig-pll-synthesizer

[7] B.C. Henderson and J.A. Cook, “Image-reject and single-sideband mixers,” WJ Communications Inc., [Online]. Available: http://www.rfcafe.com/references/articles/wj-tech-notes/ImageRej_n_SSB_mixers.pdf

[8] Analog Devices AD8307 Logarithmic Amplifier, DC to 500 MHz, http://www.analog.com/media/en/technical-documentation/data-sheets/AD8307.pdf

[9] Analog Devices AD8302 RF/IF Gain and Phase Detector, LF-2.7 GHz, http://www.analog.com/media/en/technical-documentation/evaluation-documentation/AD8302.pdf

[10] W. Kester, “Taking the mystery out of the infamous formula, SNR = 6.02N + 1.76dB, and why you should care,” Analog Devices, [Online]. Available: http://www.analog.com/media/en/training-seminars/tutorials/MT-001.pdf

CHAPTER 4

ANTENNA DESIGN

4.1. Problem Definition and Design Parameters

In any microwave imaging system, the first critical element that impacts signal fidelity is the antenna. This component has the task of effectively matching the impedance of the imaged volume to the impedance of the detector circuitry used to acquire a measurement; in this way, the antenna can be considered as a form of impedance transformer [1]. Since the propagation loss through tissues is quite large and is affected not only by conduction losses but also by the impedance mismatch between the sensing element and the tissue volume, it is essential that the antenna type is chosen carefully to ensure maximum coupling of energy into and out of the examined subject. Data extracted from the report in [2] illustrates the permittivity and conductivity typically present in different breast tissues:

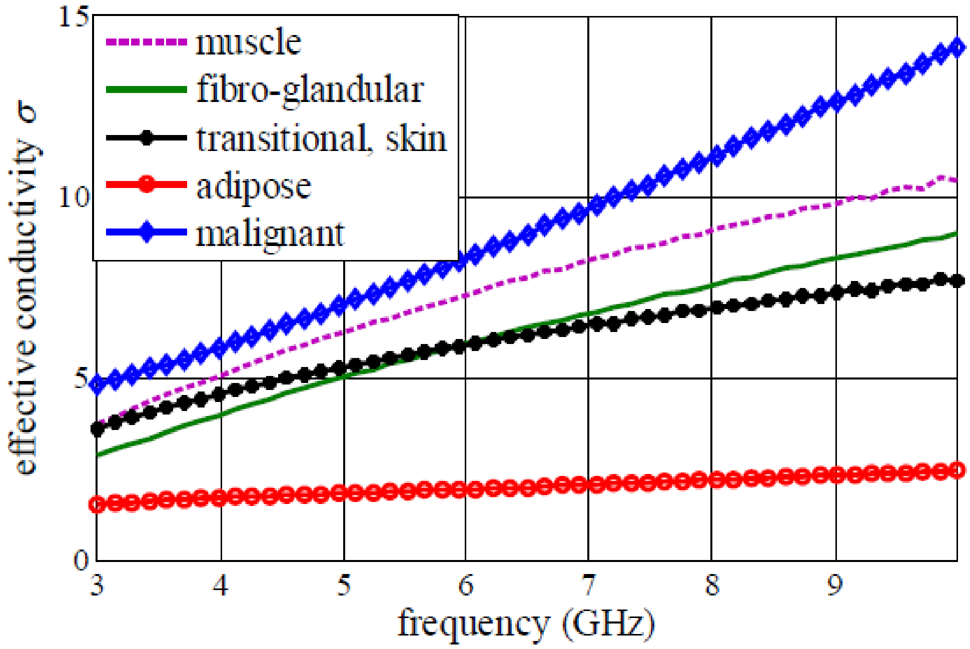

FIG. 4-1. Effective conductivity vs. frequency of various breast tissues [2].

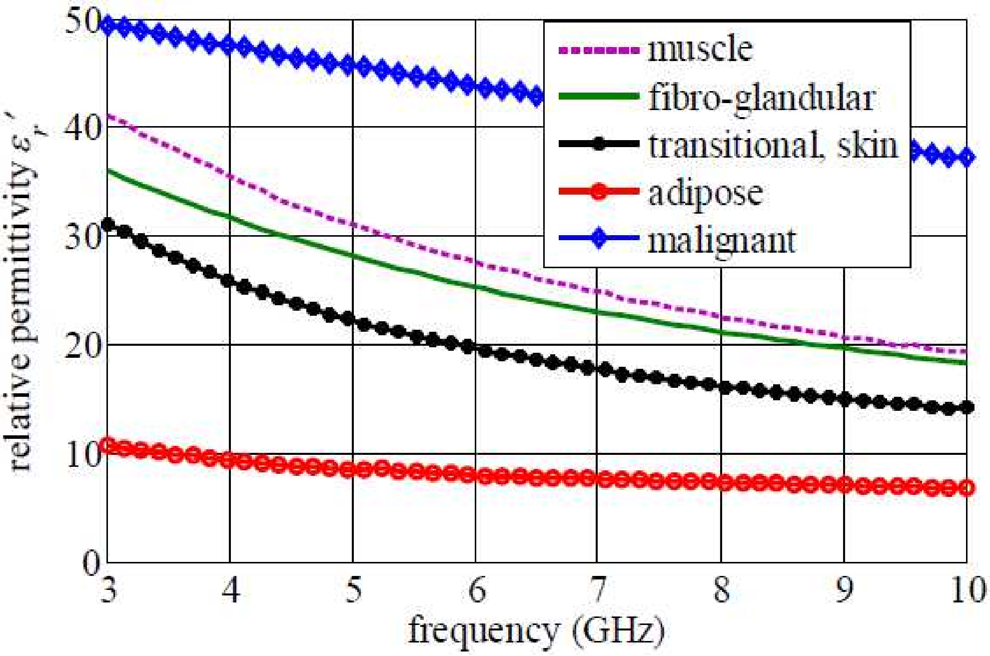

FIG. 4-2. Relative permittivity vs. frequency of various breast tissues [2].

Furthermore, the antenna design should be optimized to reduce reflections at the terminals so that minimal signal loss occurs as it transits through the detection circuitry. Careful design choices made in regard to this early stage in the signal detection enhance the system's dynamic range and signal-to-noise ratio by allowing the circuit components to use as much of the available signal as possible. The following observations are used as justification for the final antenna design choice.

Using the techniques employed in [3], it is advantageous to use a wide bandwidth of frequencies in the illuminating microwave radiation, as the use of multiple frequency measurements allows the image reconstruction algorithm to produce depth information. It is also known from experimental measurements [4] that the penetration depth of microwaves into tissues tends to decrease as the frequency of the radiation increases. Propagation losses are particularly large in breast tissue when the imaging signal frequency is increased to the tens of gigahertz. This corresponds to a decreasing penetration depth, as is shown in FIG. 4-3, where penetration depth is defined as the depth at which the intensity of the incident radiation decreases to 1/*e*, given *e* is the base of the natural logarithm [5].

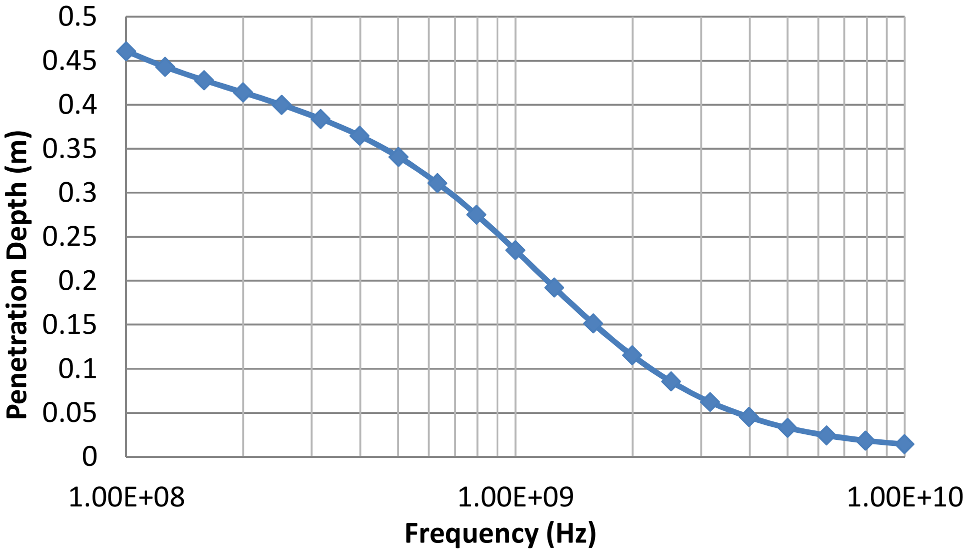

FIG. 4-3. Breast fat penetration depth vs. frequency [4].

Likewise, the wavelength of the electromagnetic radiation is inversely proportional to its frequency, and is also inversely proportional to the square root of the permittivity of the medium in which the radiation propagates [5]. Following the derivation in [6], the achievable resolution in the cross-range of an image produced using near field microwave holography varies directly with the wavelength of the radiation. Therefore, it is possible to resolve smaller features in an image by irradiating a subject with higher frequency radiation. It is worth noting that cross-range resolution comparable to 1 cm or lower can be obtained in breast tissues, assuming an average relative permittivity of at least 10, by using microwaves within the ultra-wideband (UWB) range of frequencies (3.1 GHz to 10.6 GHz). Thus, the use of multiple frequencies allows an observer to selectively enhance resolution in exchange for sacrificing penetration depth, or vice versa.

Given these frequency dependencies in tissue imaging, a wideband antenna structure is preferable to a narrow-band design.

As described in Chapter 3, the proposed system design employs an array of imaging sensors, each being compact and closely spaced to adjacent elements. This enables dense spatial sampling with electronic switching, rather than relying solely on mechanical translation of a single probe, as is done in [3]. The small size of the individual antenna also minimizes the mutual coupling between adjacent elements of the array. This strategy is particularly relevant when considering the output of the entire imaging system. In the single output scenario described in Chapter 3, only one output port is used to capture the downconverted IF signal from all sensors. This signal is then sampled and converted by an ADC, for collection and interpretation by a computer, wherein the image reconstruction process is performed. In this architecture, only one antenna element and connected radio front-end is intended to pass an imaging signal to the output port at a time; the array elements are switched electronically by turning on and off the bias on the radio front-end components. However, the insertion losses and conversion losses of each radio front-end’s LNAs and mixers, respectively, are not infinite when the bias supplied to all other sensors is set to OFF-mode (0 volts). Thus, if an incident wave is reflected by a patch and coupled to an adjacent one, the measured signal power and phase information due to this scattering could be confused for an imaging signal. For this reason, the isolation between individual antennas, and their connected radio front-ends, is crucial, since mutually coupled signal downconverted to IF at neighbouring sensors will interfere with the signal of the single, desired sensor (in ON-bias mode) in each spatial sampling instant. This interference at the IF port may be constructive or destructive, and thereby alter the reported magnitude and phase of the received signal for a particular sensor. Choosing an antenna element that minimizes this parasitic coupling is therefore critical in maintaining high image fidelity for this system architecture.

For accurate reconstruction of biomedical images using microwaves, it has been demonstrated by Larsen and Jacobi [7] that varying the polarization of the incident radiation with respect to the receiver antenna's polarization can be used to elucidate certain geometric features of an object that may normally be obscured. For instance, in [7], imaging is performed on canine kidneys with two distinct polarizations – co-polar and cross-polar. The transmitting and receiving antennas are either in full polarization match (co-polar), or orthogonal (cross-polar). It is observed that in cross-polar measurements, the piecewise linear structures of the canine kidney are more visible with enhanced contrast, whereas the co-polar measurements tend to balance renal cortical lobulations. By this demonstration, it is desirable to choose an antenna type that can either be fixed in polarization with simple modification, or altered dynamically with electronic switching.

Finally, considering both the ease and repeatability of fabrication, the system's receiver antenna design should be a printed variant. By using modern printed circuit board (PCB) manufacturing techniques, the variation in return-loss for all antenna elements can be minimized, yielding more uniformity in sensor performance across the array. This repeatability is invaluable when multiple arrays of the same antenna structure may be used in different modules of the system architecture, as is demonstrated in the wireless LO signal section of the system proposed in Chapter 3. Printed antenna structures also have the distinct advantage of offering lower cost, since the techniques employed often consist of photolithography and etching on mass-produced circuit board substrates. This strategy bypasses the process of computer-controlled milling, which can be extremely costly when tight design tolerances must be observed. Additionally, by printing the antenna structure entirely on conventional PCB materials, the need for mixing and adding specialty dielectric epoxies and cements is avoided, thus eliminating the performance issues caused by uneven chemical concentration, application, and curing.

4.2. Design Specifications

Given these observations, the following design specifications are chosen:

Antenna element specifications:

- Operation in the ultra-wideband (UWB) frequency range (3.1 to 10.6 GHz)
- Return loss ≥ 5 dB over at least 1 GHz bandwidth near frequency of 6.5 GHz
- Compact antenna size, with maximum dimension of no more than 1 cm (comparable to desired minimum resolution)
- Polarization easily altered between adjacent elements

- Fabrication on commonly available substrate material with permittivity comparable to averaged breast tissue at microwave frequencies ($\varepsilon_r \approx 10$)

Array specifications:

- Element edge-to-edge spacing less than or equal to element size
- Elements arranged in square matrix for easy expansion of array size
- Insertion loss between adjacent elements greater than or equal to 30 dB
- Array easily shielded to prevent spurious radiation (per CRTC/FCC limits)

4.3. Design Methodology

In view of the sensor element and array specifications, circular microstrip patches are investigated as the array element type. It is shown in the literature [9]-[11] that the addition of a single shorting post, grounding the patch at a carefully chosen position, can alter the antenna's far field polarization and decrease the overall diameter for a given desired impedance. A single antenna element is simulated using Ansys HFSS version 15.0.2 [8], with its dimensions initialized for operation within the band of 4 GHz to 9 GHz, and subsequently altered via parameter sweep for optimization. The simulation is set up to run in 250 MHz steps, from 4 GHz to 9 GHz, with the Maximum Delta S convergence criterion set to 0.03 at a solution frequency of 9 GHz. The microstrip patch is modelled using perfect electric conductor (PEC) boundaries, embedded in a block of Rogers RT 6010.2LM material ($\varepsilon_r = 10.2$), and connected to a modelled RG-178 coaxial line, using Teflon dielectric and PEC core/cladding (shield simulated with PEC boundary on outer surface of dielectric). This coaxial line type is chosen because of its small dimensions (1.8 mm shield outer diameter, 1.68 mm dielectric outer diameter) and because the line's characteristic impedance matches the desired system impedance of 50 Ω. The coaxial line is driven by a wave port, leaving the HFSS radiation box (volume in which discretization and simulation are performed) through a ground plane (PEC boundary).

The antenna element is placed against a block of custom defined dielectric, with $\varepsilon_r = 10$ and $\tan\delta = 0.5$. This block represents an imaging phantom made by Emerson and Cuming, used in the Computational Electromagnetics Research Laboratory at McMaster to represent the averaged electrical properties of breast tissue. The block is assigned a thickness of approximately one quarter-wavelength at the lowest frequency of simulation (4 GHz), as is recommended by Ansys in the HFSS help guide [8]. The phantom's exterior walls are set as perfectly matched layer (PML) boundaries, using the PML Setup Wizard, with the uniform HFSS-calculated thickness of 4.537 mm, setting the minimum frequency of free radiation to 4 GHz, and using the HFSS-determined minimum radiating distance of 9.875 mm.

Once an individual patch is designed, a small 3x3 array of patches is simulated to examine the impact of the neighbouring elements on a single antenna. The inter-element spacing is adjusted in the optimization step to minimize the return-loss at the desired centre frequency of 6.5 GHz while keeping the maximum separation distance as small as possible.

Since each patch antenna is meant to behave as an imaging sensor, it is critical that the sensor is designed in such a way as to minimize its scattered radiation to neighbouring elements, as explained earlier. By carefully choosing the edge-to-edge patch spacing of the array, a compromise is made between the far field directivity, return loss, and insertion loss between neighbouring elements in the final solution.

The circular patch antennas are investigated further for polarization. By adjusting the angular position of the shorting post, two different polarizations can be obtained: left-handed circular (LHC) and right-handed circular (RHC). The angular positions for best return loss and greatest difference in LHC/RHC polarizations along the z-axis (boresight) are determined by parameter sweep. In the case of circular microstrip patches, the shorting post is easily manufactured using a drilled via hole in the printed circuit board substrate.

4.4. Initial Antenna Design

As a first attempt, a single circular patch embedded in Rogers RT 6010.2LM material is developed in Ansys HFSS. The patch height is chosen as approximately 0.05λ (5% of wavelength) at 6.5 GHz in the dielectric, as Balanis suggests in [12]. The patch is placed against the imaging phantom as described in the design methodology, Section 4.3. As suggested by the design formulae in [12] using the Cavity Model approach for circular patches, the patch radius a should be approximately 4.2 mm for a patch height of 0.722 mm:

$$0.05\lambda = 0.05\cdot\frac{c_0}{f\sqrt{\varepsilon_r}} = 0.05\cdot\frac{299792458}{6.5\cdot 10^9\cdot\sqrt{10.2}} \cong 0.722\,\text{mm}. \tag{4.1}$$

$$\left(f_r\right)_{110} = \frac{1.8412}{2\pi a\sqrt{\varepsilon_r}\sqrt{\mu_0\varepsilon_0}};\; f_r = 6.5\cdot 10^9\ \text{Hz},\, \varepsilon_r = 10.2. \tag{4.2}$$

$$a = \frac{1.8412c_0}{2\pi(6.5\cdot 10^9)\sqrt{10.2}} \cong 0.00423\,\text{m}. \tag{4.3}$$

The initial feed-point position is chosen by requiring that the cross-section of the coaxial line be completely concealed by the metallic patch, so that the shield and core of the line are isolated from the imaging volume, minimizing spurious radiation. Using RG-178 with a dielectric outer diameter of 1.68 mm, the radial position of the coaxial cable centre conductor is therefore set to 3.36 mm. It is shown later in the optimization section of this antenna design that this location indeed yields excellent return loss within the band of interest.

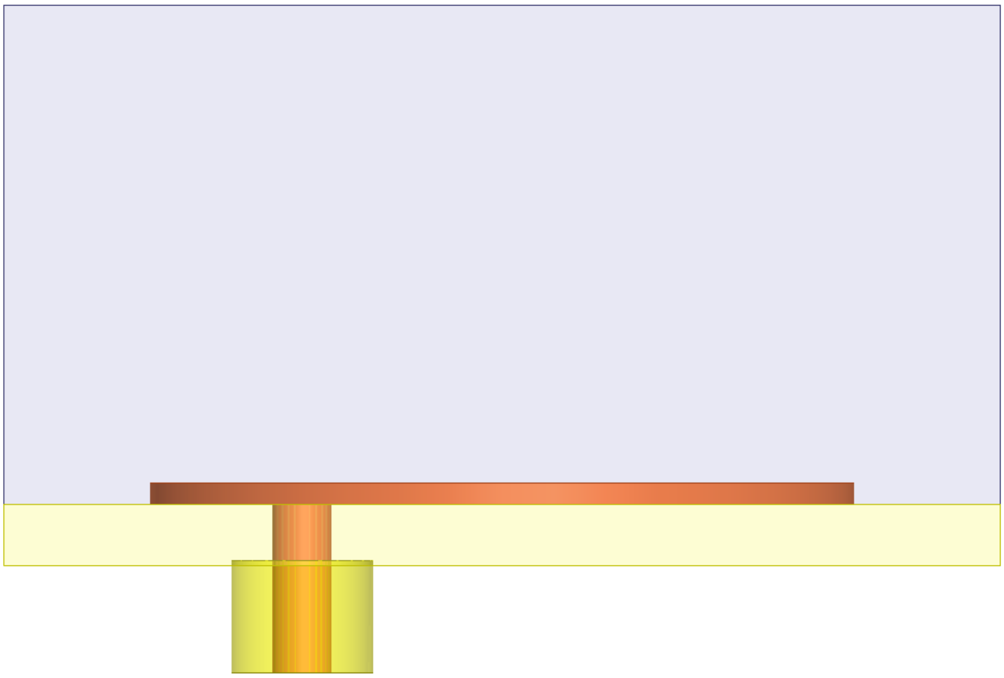

FIG. 4-4. HFSS side view of single patch, initial step; PEC shown in orange, Rogers high permittivity PCB substrate in light yellow, coaxial cable dielectric in yellow, imaging phantom in light blue (Note: diagram shows non-zero patch thickness for illustrative purposes only – simulation is performed using a zero thickness PEC boundary).

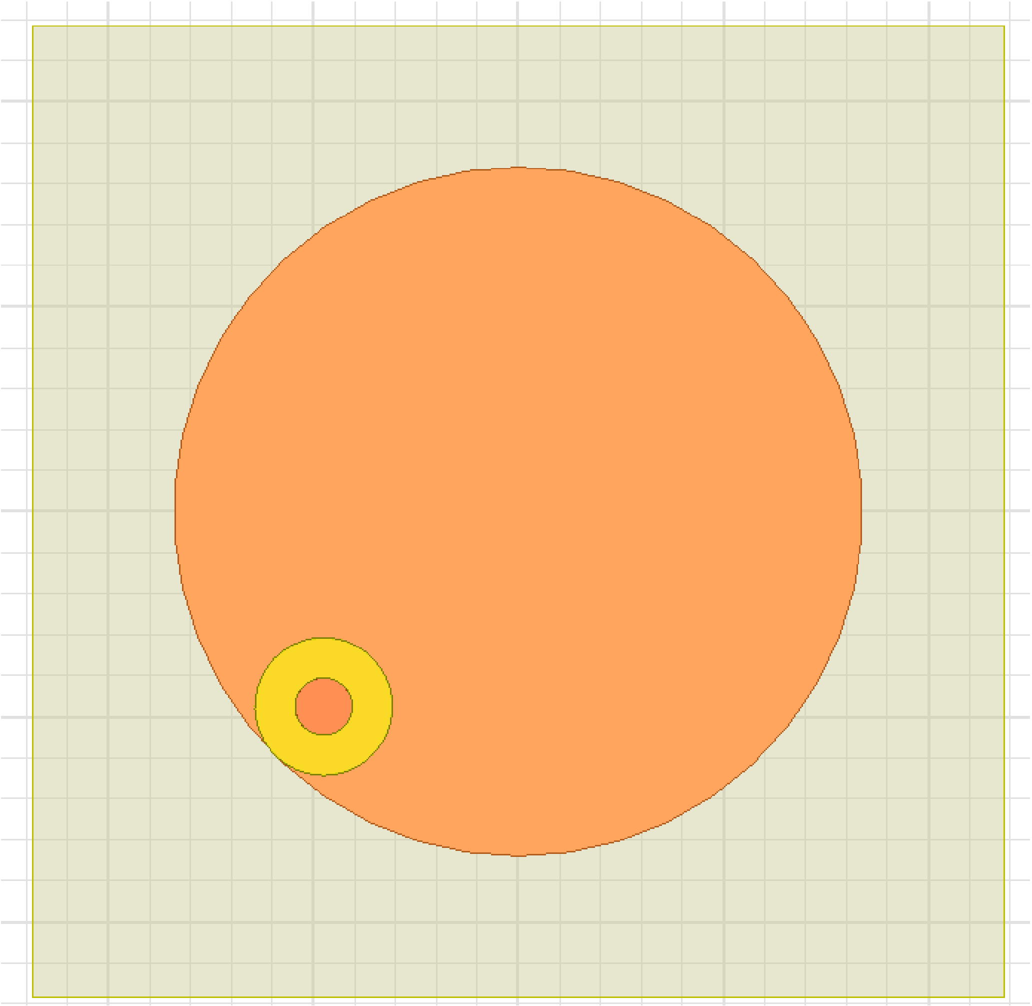

FIG. 4-5. HFSS bottom view of single patch, initial step; coaxial feedpoint chosen at boundary of patch.

4.5. Antenna Optimization

A single circular patch element is tuned in 5 optimization steps:

STEP 1: The feedpoint is varied radially from the centre of the patch to the perimeter; displacement is found by parameter sweep, with the constraint that the entire thickness of the coaxial cable be contained within the surface area of the patch – no coaxial cable dielectric should protrude beyond the circumference of the patch, to minimize spurious radiation

STEP 2: A shorting post is placed at the perimeter of the patch in a fixed location and the diameter of the patch is varied by parameter sweep; patch diameter is swept from 5 mm to a maximum of 10 mm in 9 steps; diameter is chosen for best far field boresight total directivity

STEP 3: Shorting post radial position is varied by parameter sweep, to maximize the separation of left-hand and right-hand circular far field directivities in the antenna boresight

STEP 4: Shorting post angular position is varied by parameter sweep, to maximize return loss and far field boresight directivity separation between left-handed and right-handed polarizations

STEP 5: Substrate thickness is altered for a fixed set of manufacturer-specified thicknesses to evaluate the substrate choice for best return loss and total far field directivity

Notice that the far field directivity is included in the optimization goals. This is done so that the antenna's polarization can be determined in simulation. Since the antenna is intended to be used in a dual polarization scenario, it is important that the polarization be accounted for early in the optimization stages. By using far field parameters, the antenna can be adjusted to present the greatest separation of left-handed circular from right-handed circular components for a given polarization mode. Although the antenna is used in both near and far field regions during imaging, antenna tuning performed with far field goals is simpler; a discrete volume of space must be defined in HFSS in which to perform near field calculations, and this volume would likely need resizing to accommodate changing patch sizes during optimization.

Step 1: Feedpoint variation

In the first optimization step, the feedpoint radial location is defined as follows:

$$x_{\text{feed}} = -\frac{d_{\text{patch}}}{\sqrt{8}} + r_{\text{feed}} \quad y_{\text{feed}} = -\frac{d_{\text{patch}}}{\sqrt{8}} + r_{\text{feed}} \,. \tag{4.4}$$

where x_{feed} and y_{feed} are the x- and y-coordinates of the feedpoint, d_{patch} is the diameter of the patch, and r_{feed} is a radial distance parameter to be varied in the optimization of feedpoint location. These formulae are used to position the centre conductor of the coaxial line exactly on the perimeter of the patch when r_{feed} is set to zero. The parameter r_{feed} is varied within the following value range:

$$r_{\text{feed}} = \left(\frac{0.84\,\text{mm}}{\sqrt{2}}, \frac{d_{\text{patch}}}{\sqrt{8}} \right). \tag{4.5}$$

The first value places the coaxial feedpoint near the patch perimeter, ensuring that the entire coaxial dielectric is contained within the perimeter of the patch. The second value simply resets the x- and y-coordinates of the feedpoint to zero, placing the feedpoint directly in the centre of the patch. FIG. 4-6 reveals the variation in return loss with choice of feedpoint, for 5 different positions. A value of $r_{\text{feed}} = 0.594$ mm is chosen to yield the best return loss.

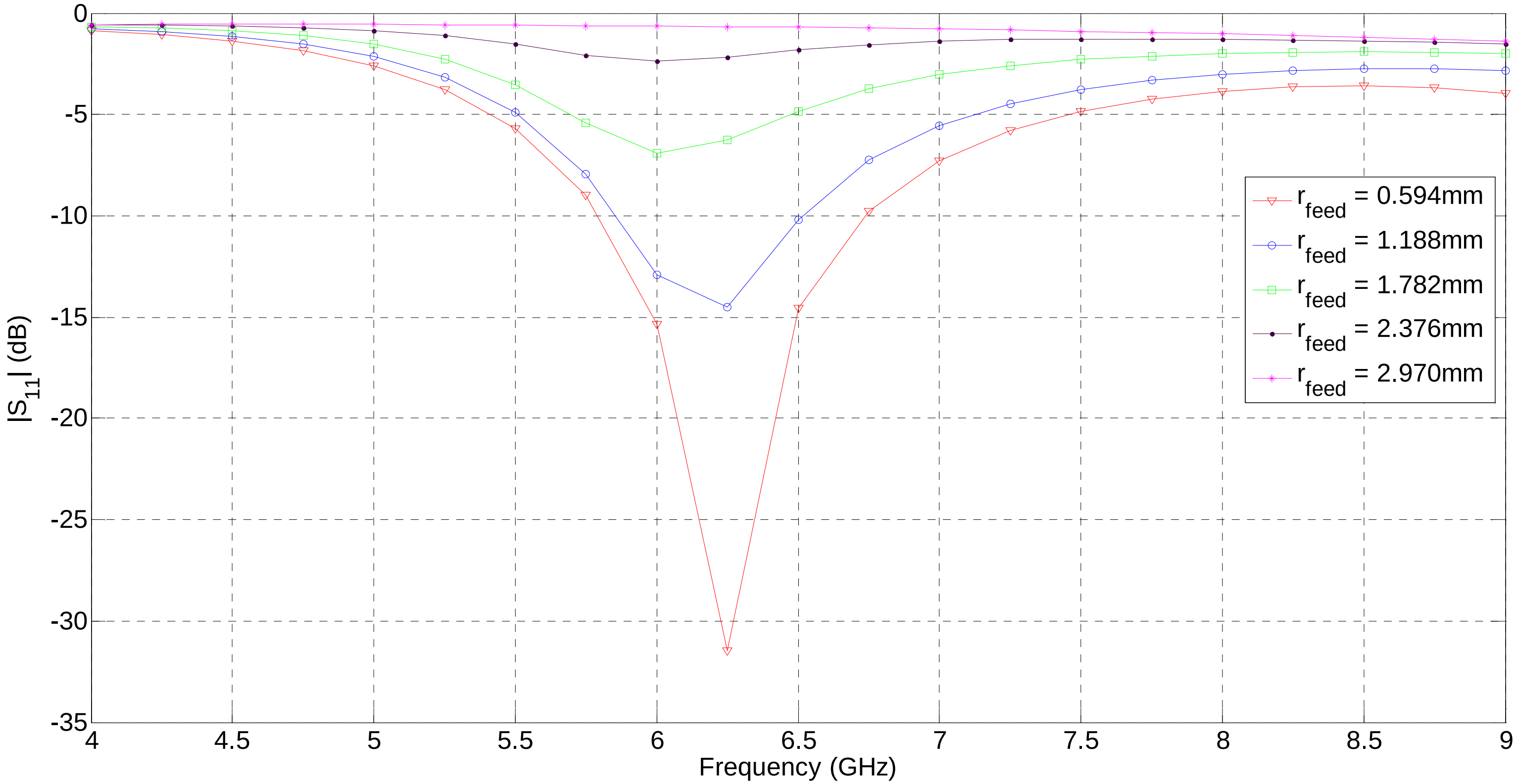

FIG. 4-6. Return loss vs. frequency for 5 separate feedpoint radial positions.

Step 2: Diameter variation with fixed shorting post

In the second optimization step, a shorting post of 0.5 mm diameter is added to the antenna structure using a PEC cylinder, located as follows:

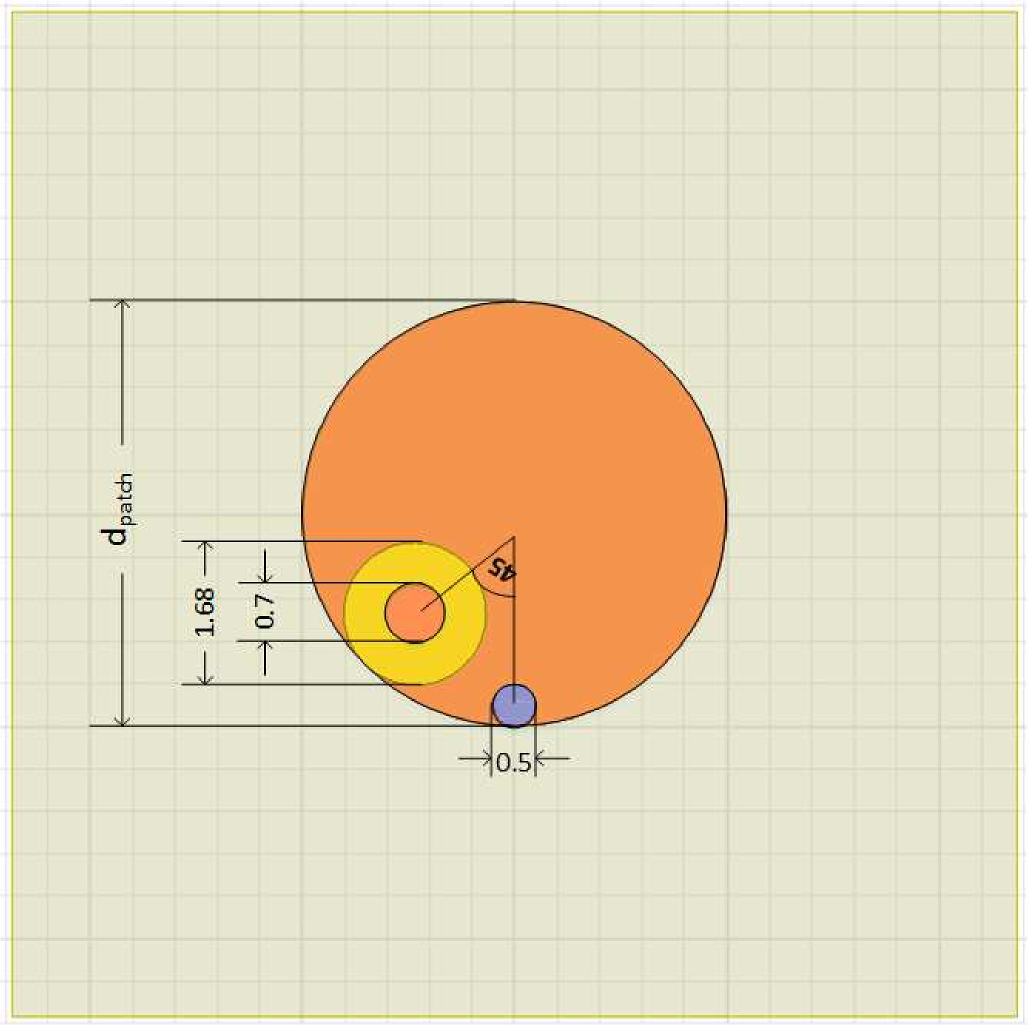

FIG. 4-7. Diagram of patch antenna during patch diameter optimization, bottom view; all dimensions given in units of mm and degrees; shorting post depicted in purple, displaced angularly from feedpoint by 45 degrees.

In this optimization step, the angular position of the shorting post relative to the feedpoint is preserved for every change in patch diameter. The diameter is varied between 5 mm and 10 mm, over 9 steps, in 0.625 mm increments. First, the total directivity, observed along the boresight ($\theta = 0°$, $\varphi = 0°$) of the antenna, at the system's centre frequency of 6.5 GHz is examined. As is shown in FIG. 4-8, the best performance in total directivity is found for a patch diameter of 7.5 mm. After choosing the diameter, the return loss of the patch is evaluated.

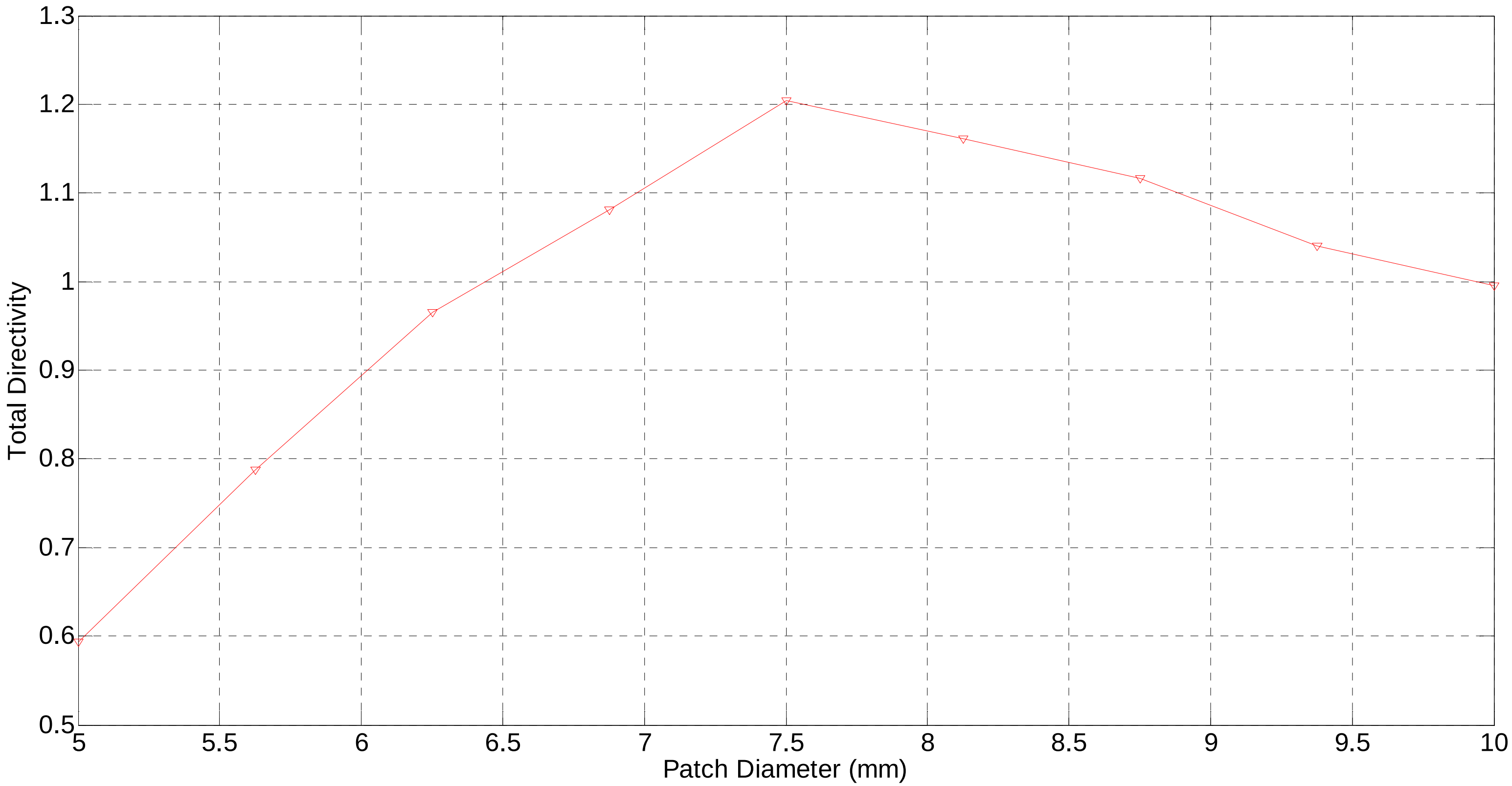

FIG. 4-8. Total directivity vs. patch diameter, evaluated at a frequency of 6.5 GHz.

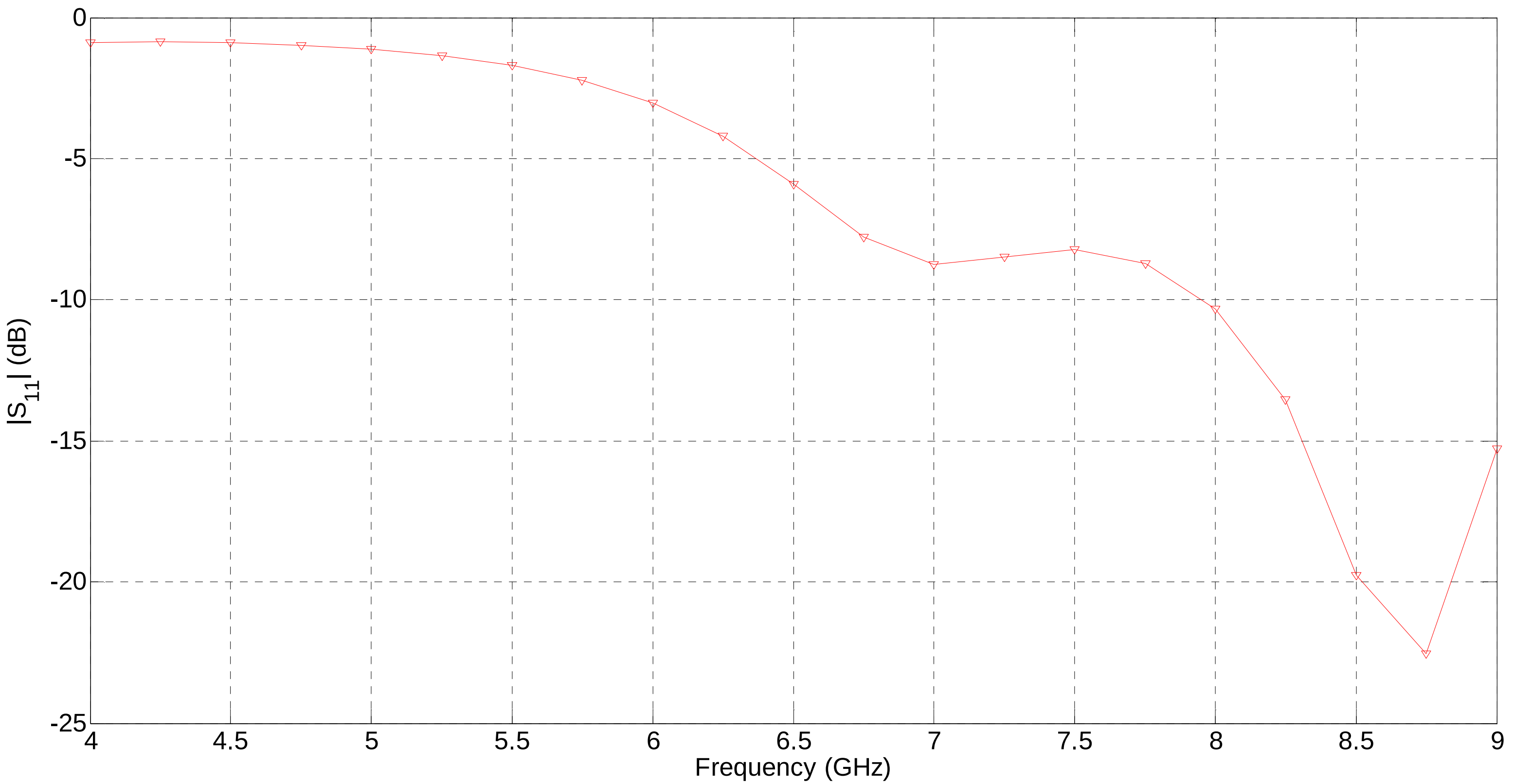

FIG. 4-9. Return loss vs. frequency for chosen patch diameter of 7.5 mm.

Step 3: Shorting post radial position variation

In this step, the radial position of the shorting post is adjusted to maximize the separation between the antenna's boresight directivities in the left-handed and right-handed circular polarization (LHCP and RHCP) components. It is shown that this separation between the two different polarization components increases as the shorting post is brought toward the perimeter of the patch. Thus, the shorting post is fixed at the perimeter of the patch antenna for high-performance operation.

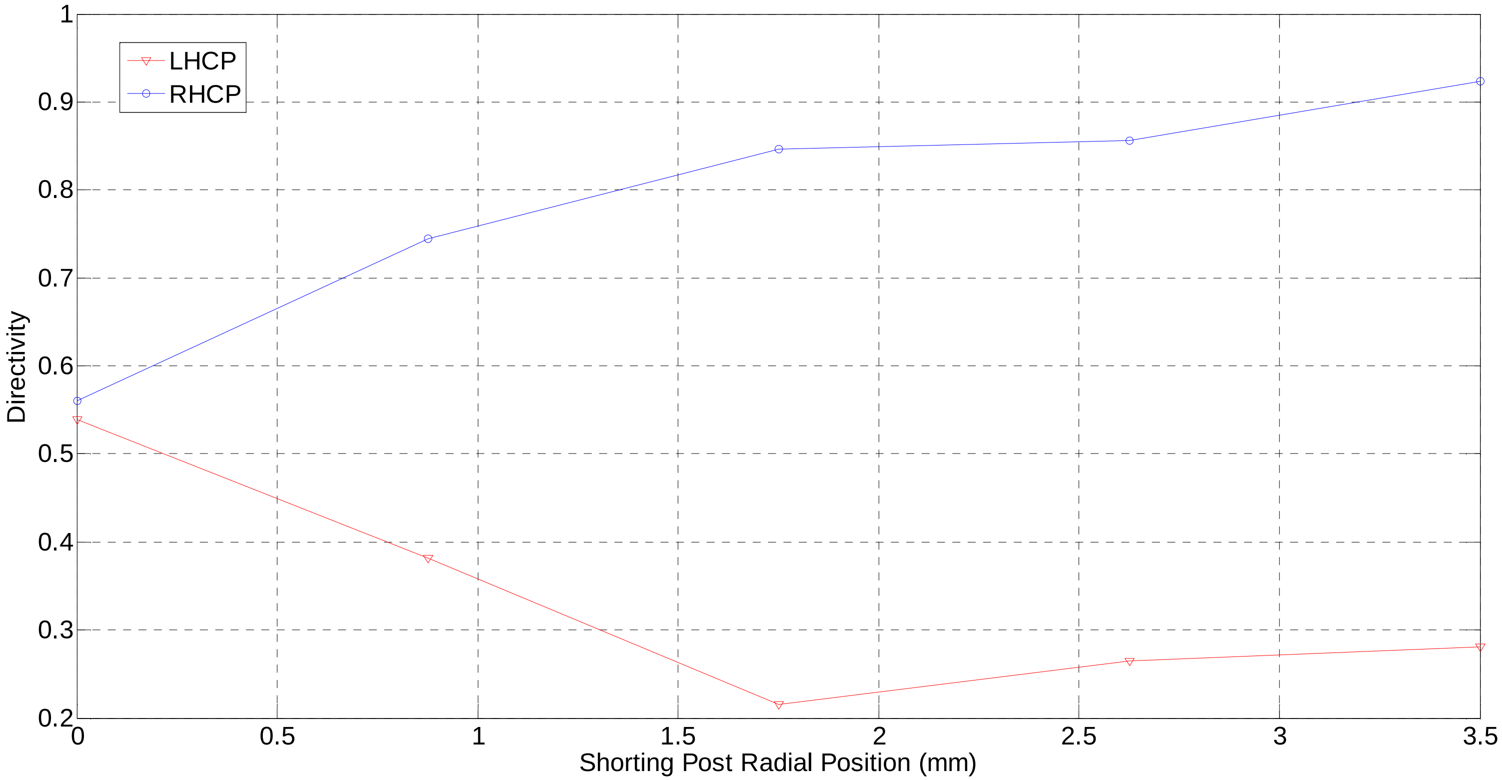

FIG. 4-10. Boresight directivity vs. shorting post position at 6.5 GHz.

Step 4: Shorting post angular position variation

In this step, the angular position of the shorting post is adjusted to optimize the return loss while maintaining large separation between the boresight LHCP and RHCP directivities. The shorting post angular position is defined in the HFSS simulation according to FIG. 4-11:

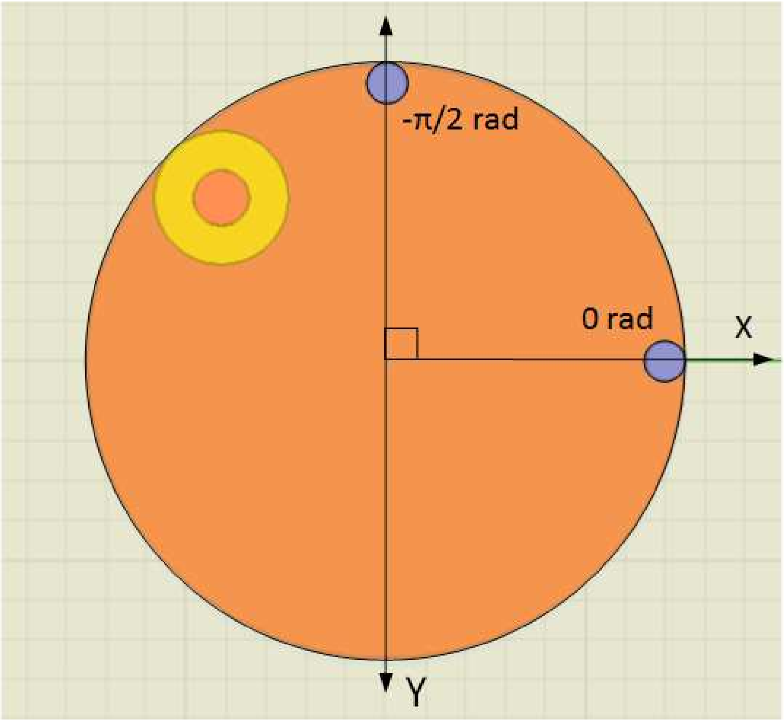

FIG. 4-11. Patch, bottom view, depicting two different angular positions.

FIG. 4-12 shows the antenna return loss versus frequency for 10 choices of shorting post angular position. Notice that although the best return loss performance can be obtained using the positions -0.5236 radians and 2.0944 radians, the difference in magnitude of the reported LHCP and RHCP directivities along boresight is much smaller than for choices of shorting post angular position closer to $-\pi/2$ radians and π radians.

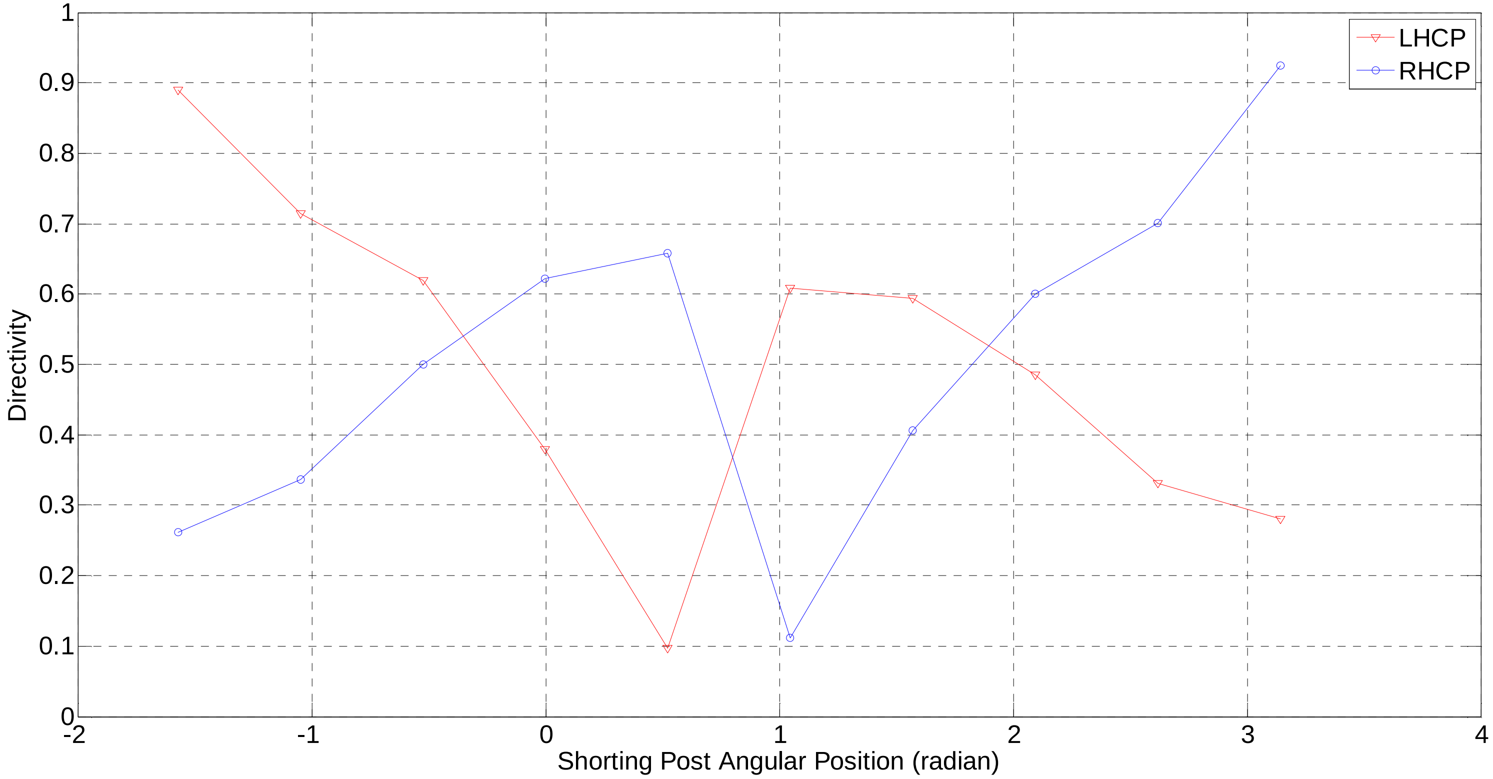

FIG. 4-12. Boresight directivity vs. shorting post angular position at 6.5 GHz.

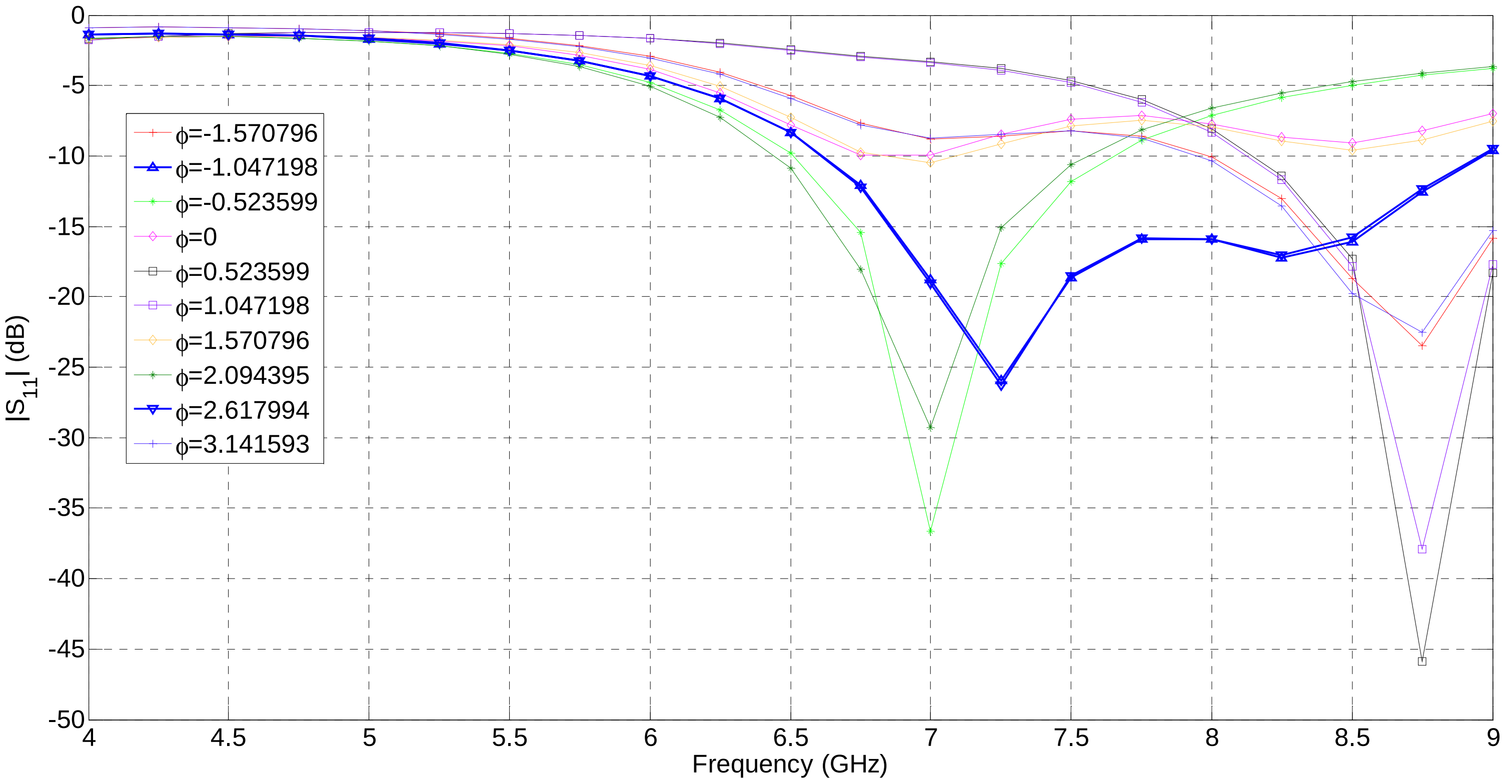

FIG. 4-13. Return loss vs. frequency for 10 shorting post angles (φ radians).

Given that excellent return loss performance (better than 10 dB) is available between 6.5 GHz and 9 GHz, combined with the significant separation between the LHCP and RHCP directivity components for the shorting post angular positions -1.047198 radian and 2.617994 radian, these are selected as the final shorting post locations in the design.

Step 5: Substrate thickness variation

In this final step of antenna optimization, the patch substrate thickness is varied over 4 distinct, manufacturer-provided values in order to optimize performance. It is shown in [13] that increasing the thickness of a microstrip patch antenna's substrate is one strategy that can be employed to improve broadband impedance match. Conversely, the use of high permittivity substrates has the reverse effect of narrowing the band of good impedance match [13]. Compensating for this reduction in bandwidth with added thickness adds further complications, since thicker substrates have a tendency to radiate surface waves [13], which are not desired here. Thus, it is important to examine the performance of the antenna structure carefully on a set of substrate thicknesses, choosing the thinnest value possible while just satisfying the primary optimization goals of broad impedance match and high LHCP/RHCP far field directivity component separation. Any added impedance matching gained from thicker substrate values may be of little use when propagation along the surface of the PCB becomes significant.

FIG. 4-14 shows the resultant return loss of the antenna with 4 different Rogers 6010LM substrate thicknesses: 0.025”, 0.05”, 0.075”, 0.1” [14]. The best return loss performance within the band of interest is obtained for a thickness of 0.05”, or 1.27 mm. Directivity is examined next. A plot of LHCP and RHCP directivity components at 6.5 GHz versus substrate thickness is also shown, and it is clear that for a PCB thickness of 0.075”, better separation of these components is available than for a thickness of 0.05”. However, in the interest of maintaining better in-band return loss performance and minimizing the strength of surface wave propagation, the final design uses a 0.05” thick substrate.

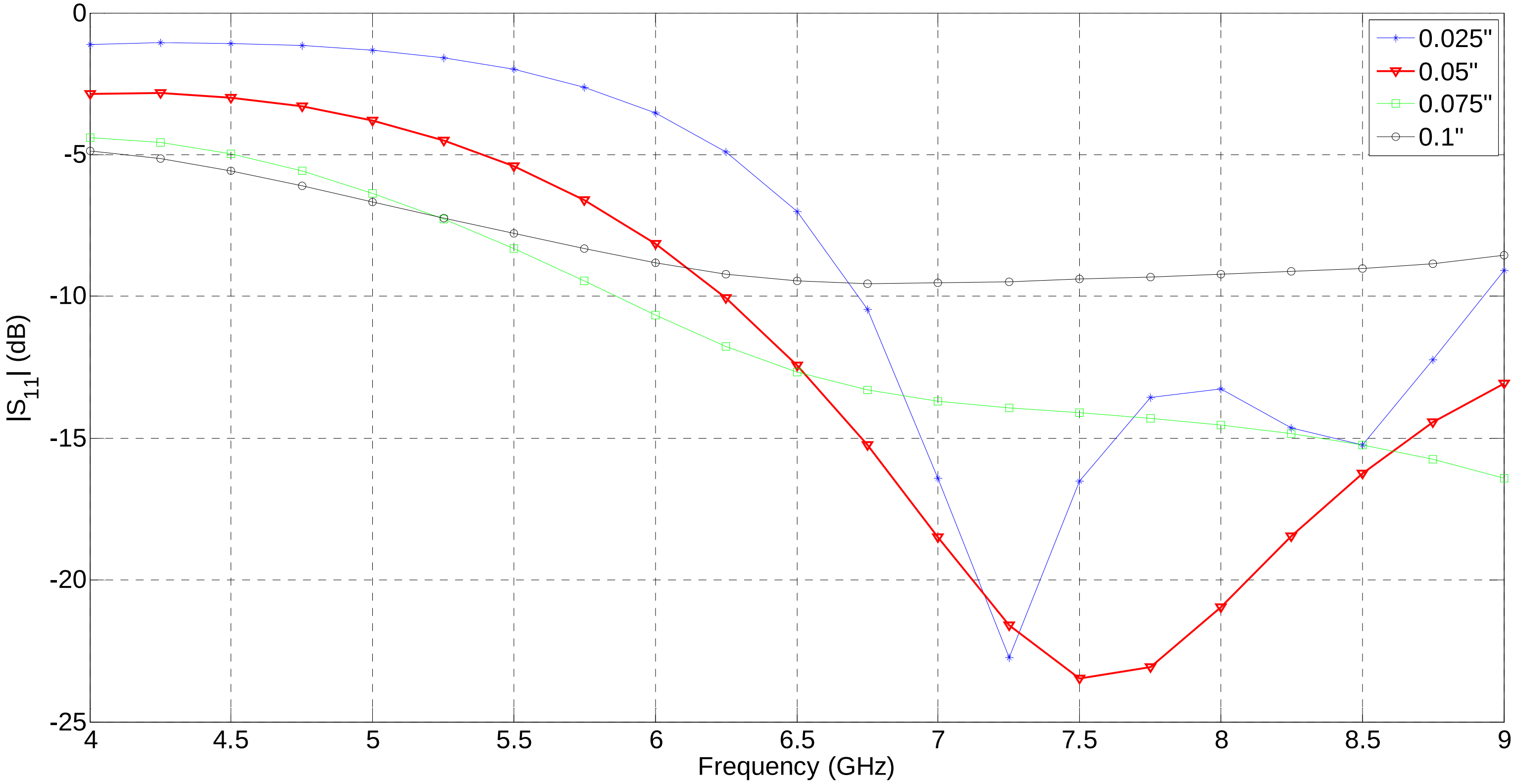

FIG. 4-14. Return loss vs. frequency for 4 different substrate thicknesses.

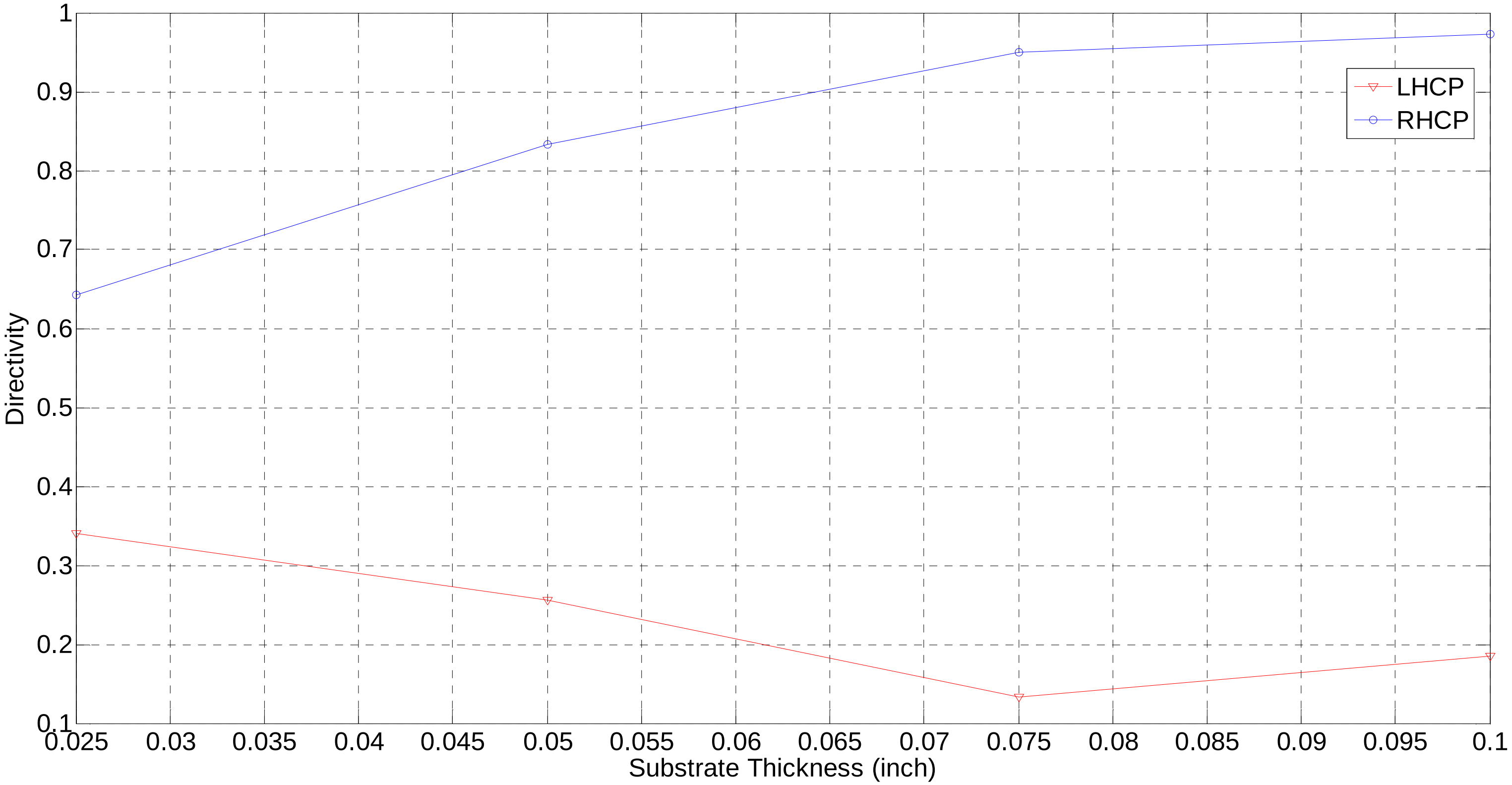

FIG. 4-15. Boresight directivity vs. substrate thickness at 6.5 GHz.

The final antenna element design is given in FIG. 4-16:

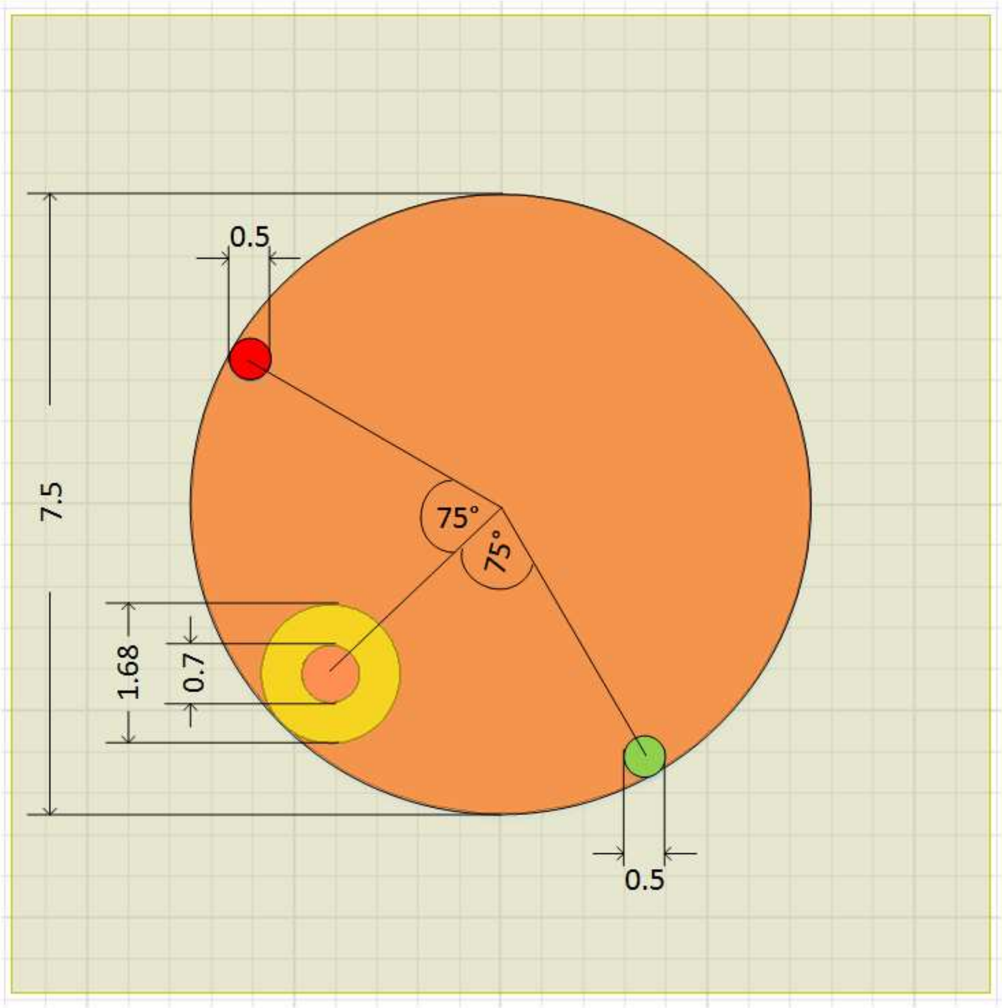

FIG. 4-16. Circular shorted patch, bottom view (dimensions in mm); two shorting post locations given for different polarizations: green (bottom right) shorting post location yields LHCP-dominant radiation, red (top left) shorting post location yields RHCP-dominant radiation.

Dual polarization capability is demonstrated by simulating the final design structure with the two chosen shorting post angular positions. Both shorting post locations are displaced 75 degrees away from the feedpoint, in opposite directions. The return loss values are in close agreement at all frequencies for both shorting post positions. The LHCP boresight directivity of the antenna with the shorting post in LHCP-dominant angular position is also nearly equal to the RHCP boresight directivity when the shorting post is moved to the RHCP-dominant angular position. Switching between the two polarization modes can be enabled in a single patch antenna element by installing PIN diodes in place of a shorting post PCB vias. When properly biased, a PIN diode can present a small impedance, on the order of 1 **Ω**, at the antenna’s operating frequency, thereby effectively shorting the patch to ground. An example PIN diode suitable for use in the PCB via dimensions is listed here [15].

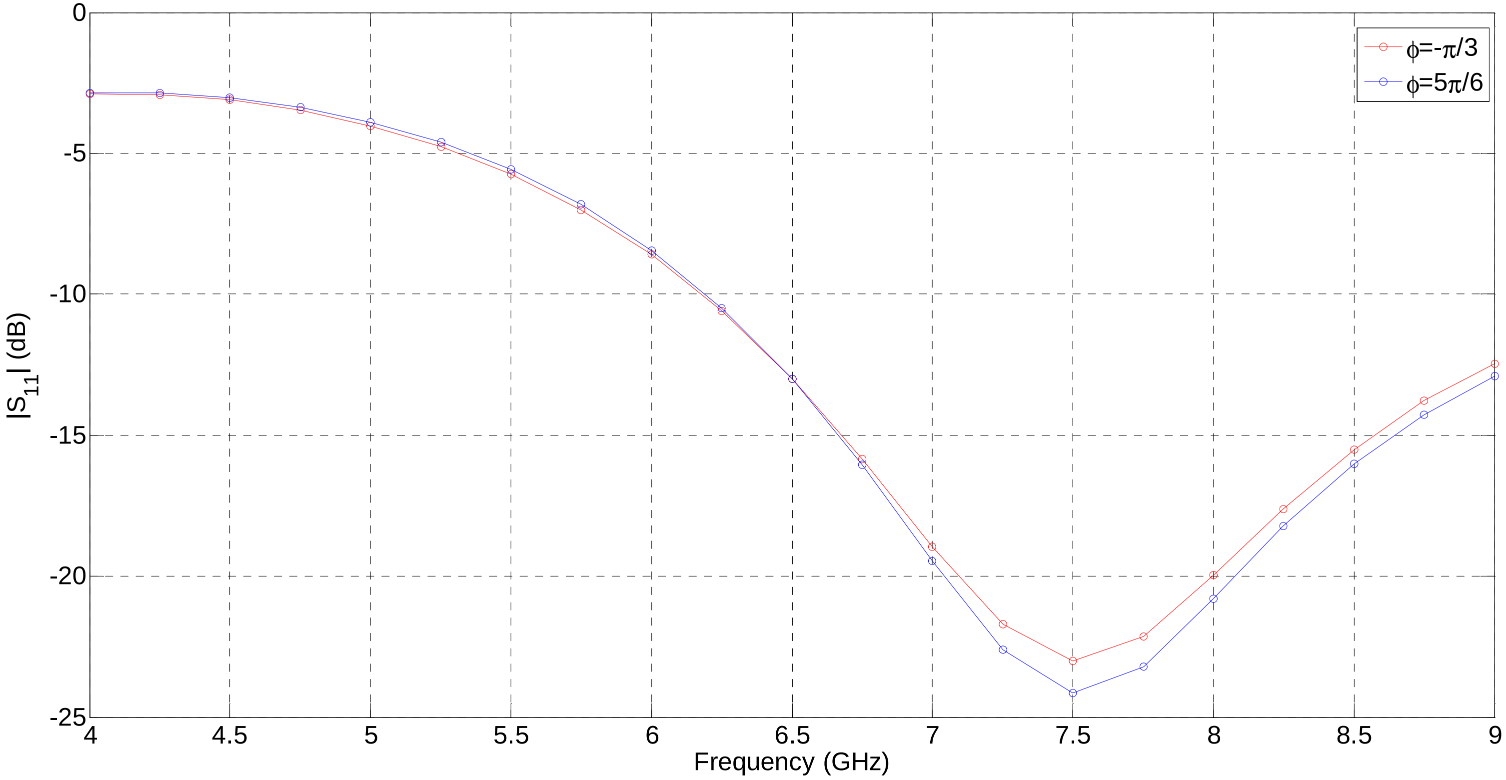

FIG. 4-17. Return loss vs. frequency, both high-performance shorting post positions.

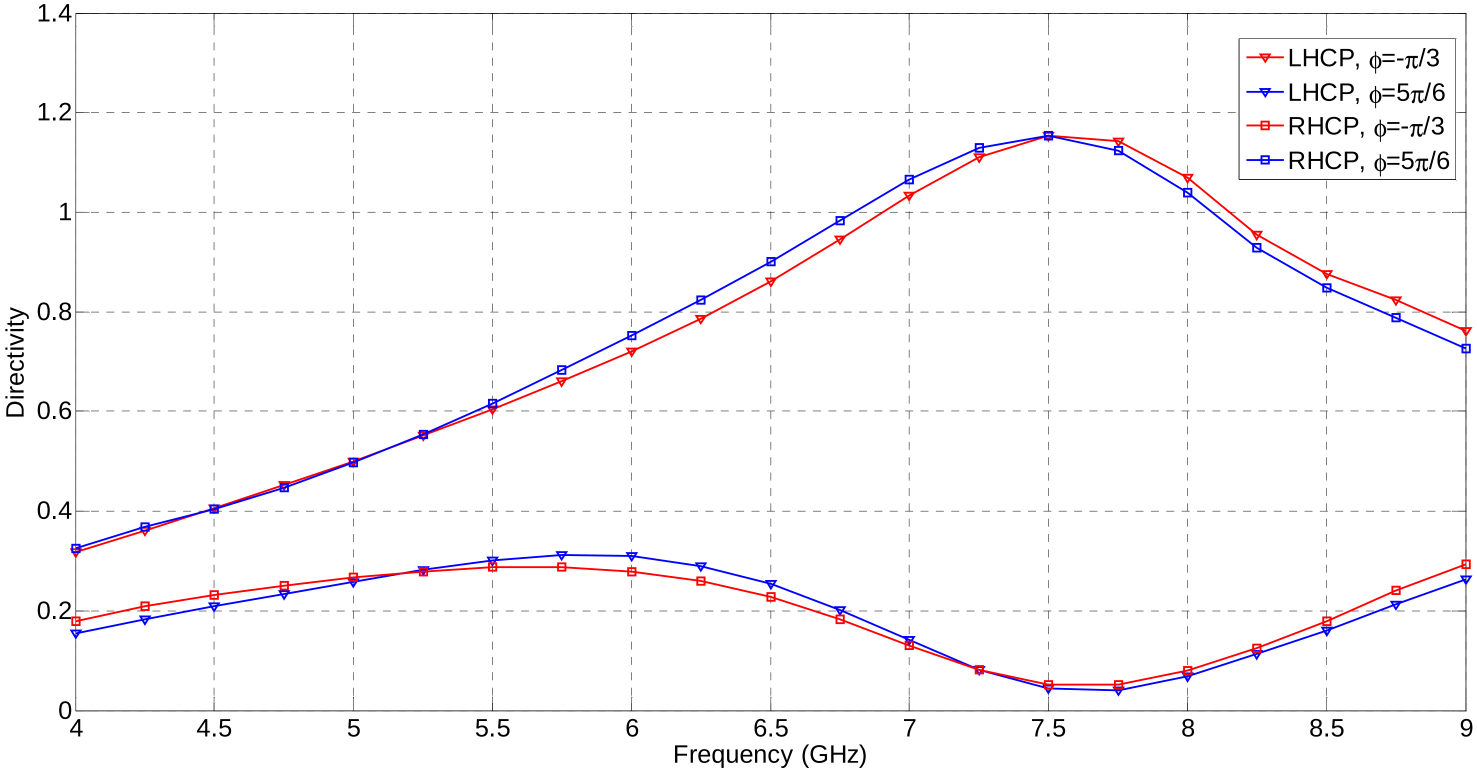

FIG. 4-18. Boresight directivity vs. frequency, both high-performance shorting post positions.

4.6. Array Optimization

The focus of this report is the design of an imaging sensor array. Once the individual sensing element has been designed, it is necessary to carefully plan the layout of the array of sensors, adjusting the inter-element spacing so as to minimize cross-coupling and maximize performance in return loss and directivity. A small array of 9 antennas, in a 3x3 arrangement, is simulated in HFSS. The maximum edge-to-edge spacing of the antenna elements is constrained to 1 cm, and is chosen for strongest inter-element insertion loss via a parameter sweep. In HFSS, the radiation boundaries are set up using perfectly matched layer (PML) boundaries, whose thickness is calculated automatically by HFSS at the maximum array element edge-to-edge spacing of 1 cm. This PML thickness is the largest calculated value for all inter-element spacing values. It is used for all values of inter-element spacing during the parameter sweep, since it is meaningful to compare the performance of the array when the boundary conditions are the same for all steps of the optimization. The array is simulated with a block of the same Emerson and Cuming phantom material described in the antenna design methodology (Section 4.3), with a thickness equal to 0.25λ in the medium at the lowest evaluated frequency of 4 GHz. All 9 elements are identical, circular shorted patch antennas, each equipped with the same coaxial cable feeding structure and shorting pin arrangement. Each antenna is connected to a wave port, defined by assigning a wave port excitation on the bottom face of the coaxial dielectric (Teflon) boundary. This is done to allow the simulation of multi-port *S*-

parameters, so that the inter-element insertion loss can be evaluated when varying the inter-element spacing.

FIG. 4-19 demonstrates the simulated return loss performance of the array for 10 different inter-element spacing values. Notice that there is little variation in the return loss when the spacing is adjusted.

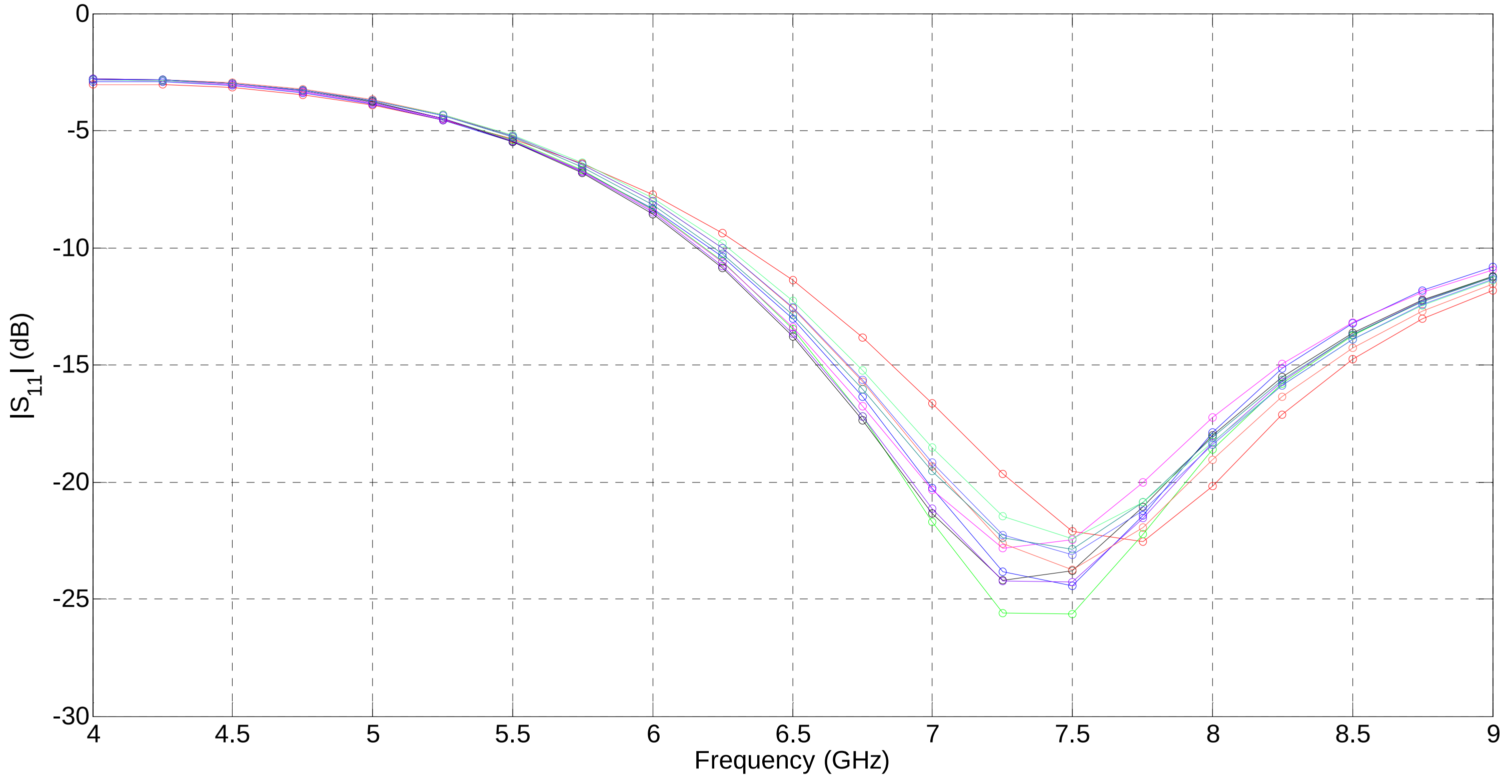

FIG. 4-19. Return loss for 10 spacing values (no legend given as return loss varies ~2 dB between different spacing values).

Next, a plot of LHCP and RHCP boresight directivities is given, showing the variation in magnitude with changing inter-element spacing. The difference between the two polarizations' directivities is relatively stable. For this reason, it is prudent to evaluate the antenna array's performance next by examining the inter-element insertion loss. In the last plot, the insertion losses are given for 4 coupling scenarios: between the centre antenna 1 and antennas 3, 5, 7, and 9, as labeled in FIG. 4-20. It is evident that an edge-to-edge spacing of at least 5 mm is sufficient to yield inter-element coupling below -30 dB, which satisfies the optimization goal stated earlier. However, in the interest of guaranteeing good performance in the prototyping stage, a spacing of 6 mm is chosen, as a margin of error is considered in the simulated data.

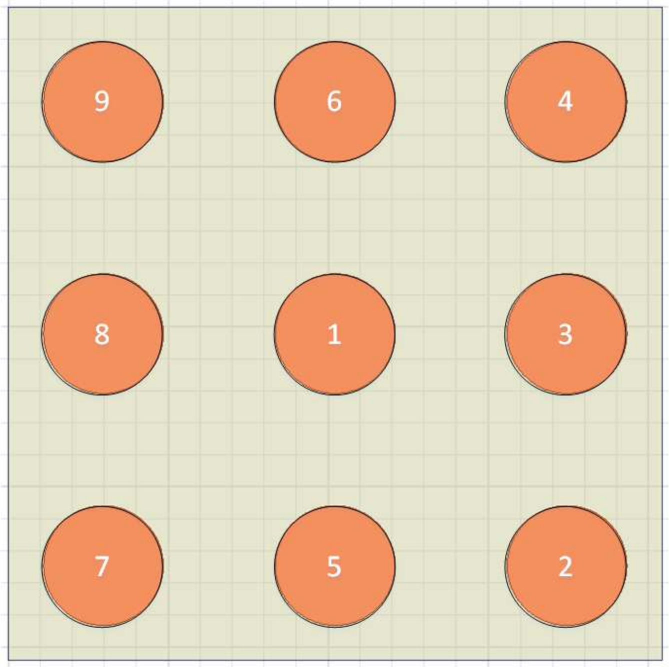

FIG. 4-20. Circular patch array, top view; elements labeled by port number.

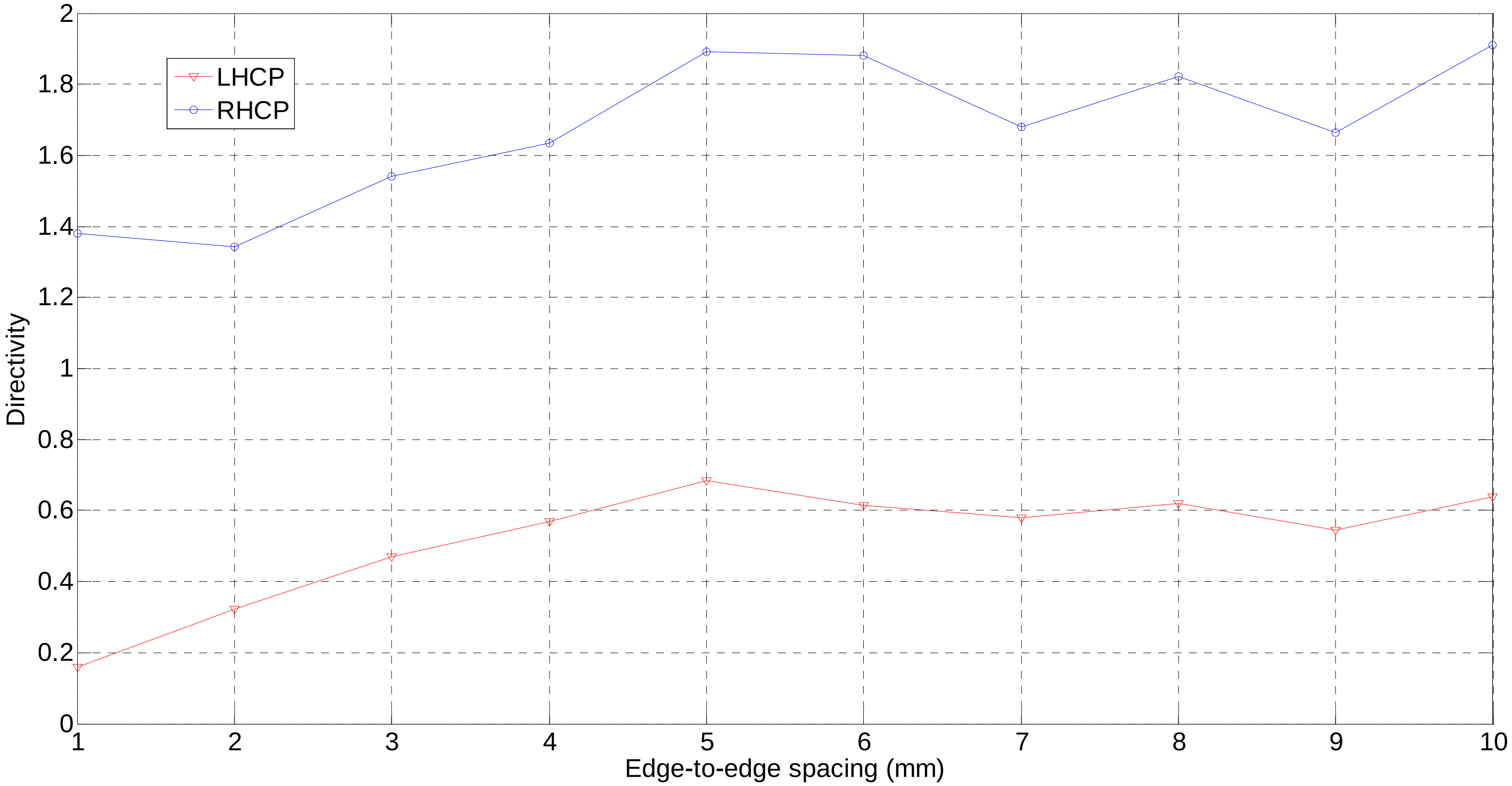

FIG. 4-21. LHCP/RHCP directivity vs. edge-to-edge spacing.

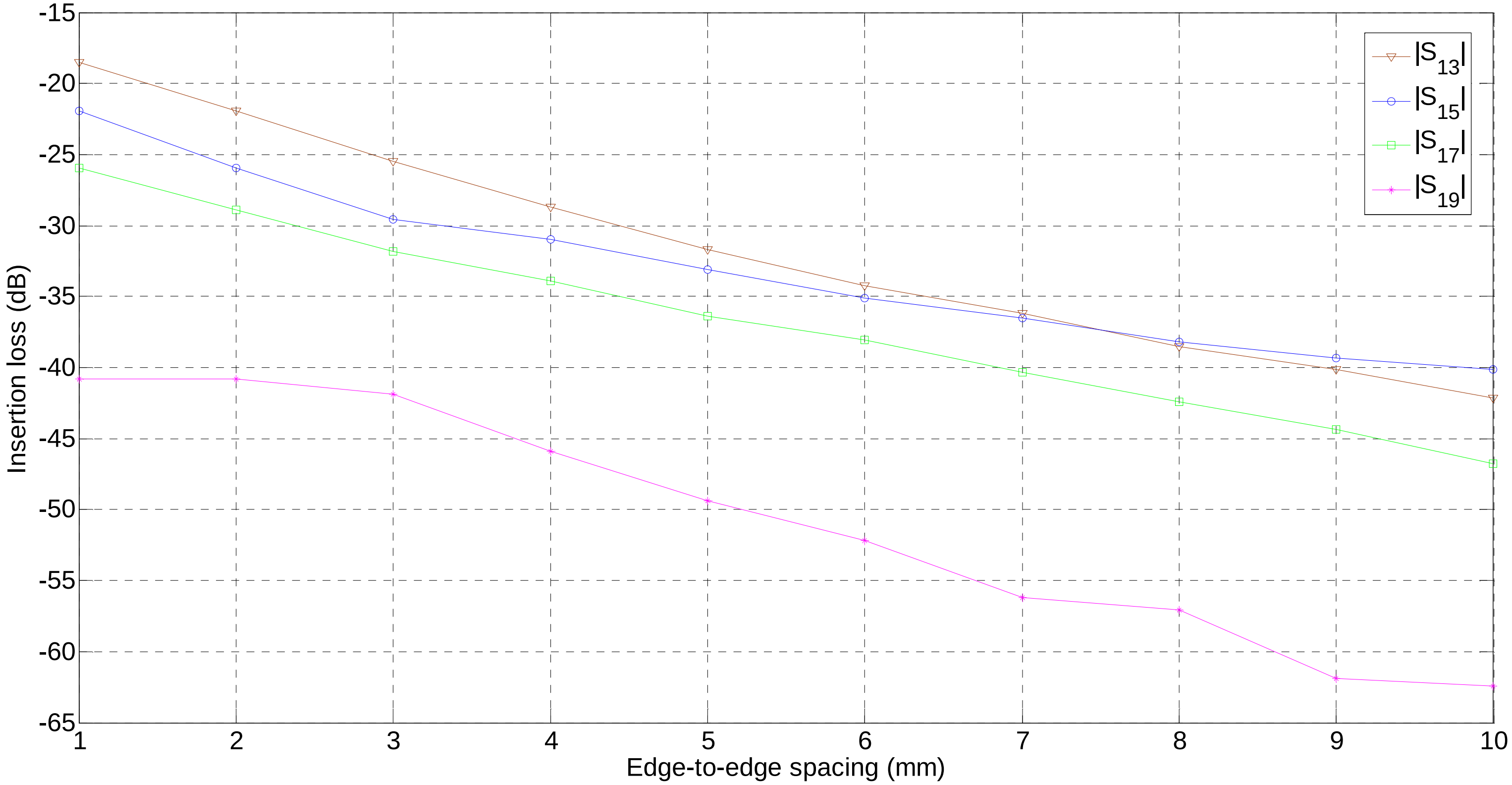

FIG. 4-22. Insertion loss between adjacent elements vs. element spacing.

4.7. Prototyping

With a design specified that yields adequate performance, the 3x3 array structure is fabricated for evaluation. A prototype antenna array is made using a 12 cm x 12 cm square section of Rogers 6010 substrate, at 1.27 mm thickness with 35 um thick copper coating on both sides:

FIG. 4-23. Picture of fabricated 3x3 antenna array.

Photolithography is used to print the microstrip circular patch elements on one side of the substrate. The feedpoint and shorting post locations are marked in the etching process for ease of machining. Only one of the two shorting post locations is drilled; a PCB via is made with the drilled hole by filling it with a solid wire of copper, soldered to the patch and to the reverse side ground plane. A PCB through-hole female SMA connector is used to feed the patch; it has 4 grounding pins, placed 90° apart on the PCB mounting side, and a long centre pin. The central conductor is tinned with solder and trimmed to an appropriate length so that it penetrates through the substrate enough to lay flush with the copper patch on the reverse side. The patch is soldered to the SMA connector centre pin. Only one patch of the 3x3 fabricated array is configured this way, and is connected to a calibrated Agilent E83638 PNA network analyzer [16], measuring return loss between 4 and 9 GHz at a resolution bandwidth of 10 kHz. The measurement is done while manually holding the antenna array down against a stack of 5 Emerson and Cuming absorbing sheets (ε_r=10, tanδ=0.5). The results of this measurement are shown in FIG. 4-25, compared with the simulated data from HFSS.

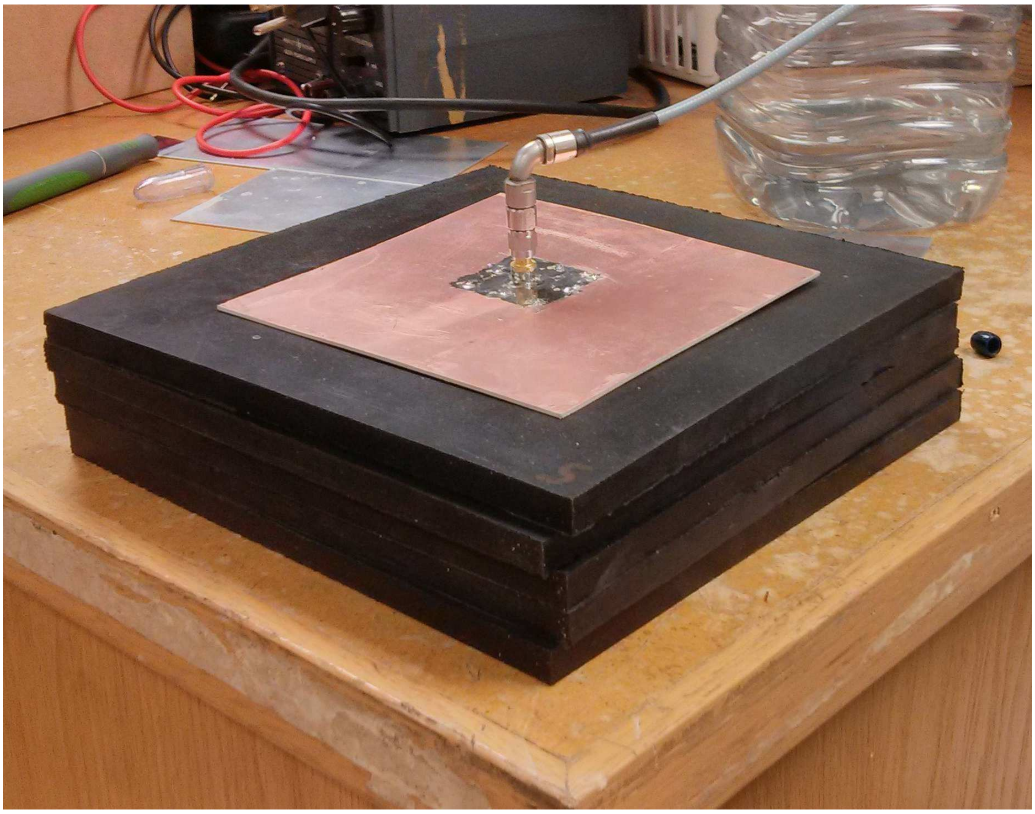

FIG. 4-24. Prototype array resting on 5-layered absorber sheet medium.

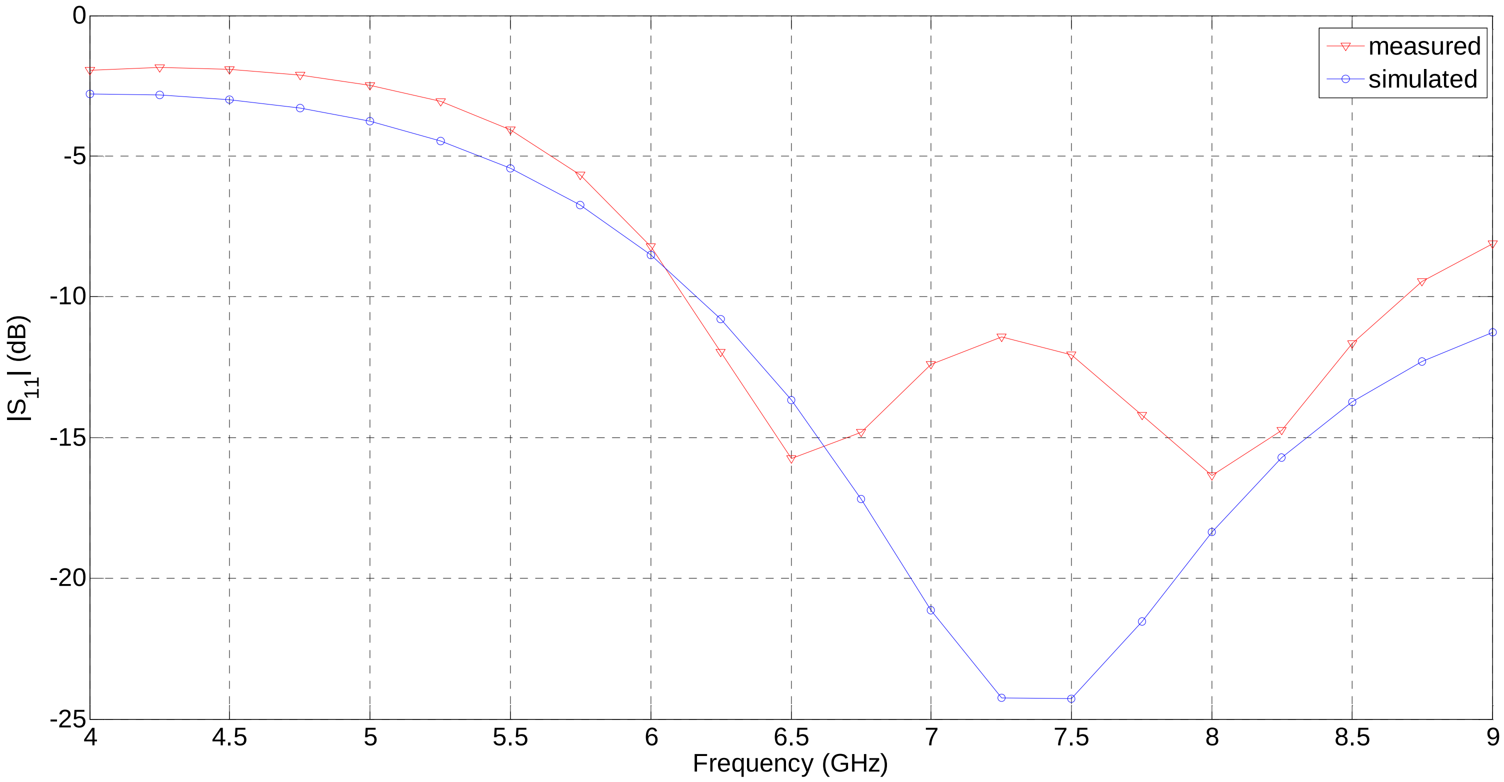

FIG. 4-25. Return loss vs frequency for measured and simulated antenna.

Notice that there is significant agreement between measured and simulated data for an appreciable section of the observed frequency band. There is, however, appreciable difference between the two data sets over approximately 1 GHz of bandwidth, centred at nearly 7.5 GHz, where the HFSS simulation overestimates the antenna’s return loss performance. This discrepancy may be due to the fact that the prototyped antenna structure has significant surface roughness due to the use of solder, and imperfect smoothing of the shorting and feedpoint pins. As a result, the antenna may not be adequately coupled to the absorber sheets, leading to some added reflection. Regardless, the measured return loss at the disputed frequencies is still below 10 dB, which exceeds the optimization goal minimum return loss of 5 dB.

4.8. Conclusions

A compact, microstrip patch design is presented for incorporation in a microwave imaging system for breast cancer screening. The design is adjusted in an imaging array configuration, keeping inter-element coupling below -30 dB while minimizing the edge-to-edge antenna spacing in the array. Return loss is better than 5 dB for a bandwidth of over 3 GHz, and better than 10 dB for a 2 GHz bandwidth in the ultrawideband spectrum. The proposed antenna structure also demonstrates dual polarization capability, altering the polarization between elements simply by changing the angular position of a PCB via, or by PIN diode. A prototype is successfully fabricated for use in experimentation.

REFERENCES

[1] H. Schantz, *The Art and Science of Ultra-Wideband Antennas.* Norwood: Artech House Inc., 2005.

[2] N.K. Nikolova, “Microwave biomedical imaging,” *Wiley Encyclopedia of Electrical and Electronics Engineering*, pp. 1–22. (published on-line Apr. 25, 2014).

[3] R.K. Amineh, M. Ravan, A. Trehan, and N.K. Nikolova, “Near-field microwave imaging based on aperture raster scanning with TEM horn antennas,” *IEEE Trans. Antennas Propagat.*, vol. 59, no. 3, pp. 928–940, Mar. 2011.

[4] D. Andreuccetti, R. Fossi, and C. Petrucci, “An Internet resource for the calculation of the dielectric properties of body tissues in the frequency range 10 Hz - 100 GHz,” (IFAC-CNR), [Online] 1997, http://niremf.ifac.cnr.it/tissprop (Accessed May 2015).

[5] D.M. Pozar, *Microwave Engineering.* 4th ed., Hoboken: John Wiley & Sons, Inc., 2012.

[6] M. Ravan, R.K. Amineh, and N.K. Nikolova, “Two-dimensional near-field microwave holography,” *Inverse Problems*, vol. 26, No. 5, 055011, May 2010.

[7] L.E. Larsen and J.H. Jacobi, “The Use of Orthogonal Polarizations in Microwave Imagery of Isolated Canine Kidney,” *IEEE Trans. Nuclear Science*, vol. 27, no. 3, pp. 1183–1191, June 1980.

[8] ANSYS HFSS, Version 15.0.2, ANSYS Inc., Southpointe, 2600 ANSYS Drive, Canonsburg, PA 15317, 2013.

[9] N. Kuga and H. Arai, “Circular Patch Antennas Miniaturized by Shorting Posts,” *Electron. Comm. Japan (part I: Communications)*, vol. 79, no. 6, pp. 51–58, Oct. 1996. [Online]. Available: http://onlinelibrary.wiley.com/doi/10.1002/ecja.4410790606/pdf. (Accessed Jan. 8, 2015).

[10] R. Waterhouse, S.D. Targonski, and D.M. Kokotoff, “Design and Performance of Small Printed Antennas,” *IEEE Trans. Antennas Propagat.*, vol. 46, no. 11, pp. 1629–1633, Nov. 1998. [Online]. Available: http://ieeexplore.ieee.org/stamp/stamp.jsp?arnumber=736612. (Accessed Jan. 8, 2015).

[11] P. Kumar and G. Singh, “Microstrip antennas loaded with shorting post,” *Engineering* 1(1), pp. 41–45, 2009.

[12] C.A. Balanis, *Antenna Theory: Analysis and Design.* 3rd ed. Hoboken, NJ: John Wiley & Sons Inc., 2005.

[13] K.C. Gupta and A. Benalla, *Microstrip Antenna Design.* Norwood: Artech House, 1988.

[14] Rogers RT/duroid ® 6006/6010LM High Frequency Laminates, http://www.rogerscorp.com/documents/612/acs/RT-duroid-6006-6010LM-laminate-data-sheet.pdf

[15] Skyworks SMP1320-079LF PIN Diode, http://www.skyworksinc.com/uploads/documents/SMP1320_Series_200047P.pdf

[16] Agilent E83638 PNA network analyzer

CHAPTER 5

RADIO RECEIVER FRONT-END DESIGN

5.1. Introduction: Problem Definition

As described in Chapter 3, the complete imaging system performs switching of the sensor array by controlling the bias to the integrated receivers. Each antenna is paired with an individual receiver, consisting of two cascaded low-noise amplifiers (LNAs) and a mixer. Both the amplifiers and the mixing element provide gain. Further, the two amplifiers together provide significant insertion loss (approximately 40 dB) of the imaging signal when their bias is OFF (0 V applied). This property is useful as it can be exploited to replace the conventional RF switch component used in conventional array-based imaging systems [1]-[3]. The property is not limited to the amplifiers – the active mixer component also yields significant conversion loss at the IF when its bias is set OFF. Switching the bias ON and OFF of active mixers has been exploited before as an effective method of switching between signal paths [4].

This section describes the design of the radio receiver front-end. The module is constructed with inexpensive, surface-mount microwave devices on printed circuit boards with coplanar waveguide transmission lines. Specifications are given in the next section, followed by component choices and a design. An experimental prototype is built for evaluation.

5.2. Design Specifications

The following specifications are given as a guideline for component selection. They are chosen based on the performance parameters described in Chapter 2. A prototype receiver is constructed and evaluated with measurements on a spectrum analyzer to compare with the manufacturer-quoted performance.

Specifications:

- Operation in the ultra-wideband range (3.1 GHz to 10.6 GHz)
- Active mixer with conversion gain
- Low-noise components
- Maximum component dimension less than microstrip patch diameter
- Dynamic range (sensitivity to 1-dB compression) ≥ 100 dB
- Difference between IF output power in ON/OFF modes ≥ 100 dB

For design compactness, the maximum dimension of any component in the radio receiver is restricted so that the entire module can be designed for integration below the ground plane of the antenna array. Components with low noise figure should be chosen in an effort to maximize receiver sensitivity.

5.3. Design Methodology

Observing the specifications established in the previous section, candidate components are chosen for possible inclusion in the final design. The following two LNAs are found capable of satisfying the receiver specifications:

- Avago VMMK-3803
- Mini-circuits PMA3-83LN+

The Avago VMMK-3803 [5] is an LNA in a surface-mount 0402 package (0.5 mm x 1 mm) designed for use between 3 GHz and 11 GHz. It features a 1.5 dB typical noise figure (at 6 GHz). It has approximately 17 dB of gain in the band of interest and a 1-dB output compression point of approximately 6 dBm with a bias of 3 V.

The Mini-circuits PMA3-83LN+ [6] is an LNA in a surface-mount 3 mm x 3 mm package, designed for operation between 0.5 and 8 GHz with a typical noise figure of 1.4 dB (at 4 GHz). It has approximately 20 dB of gain across the band and features a 1-dB output compression point of 21.5 dBm. This part has only recently been announced by the manufacturer, and was not selected for use in the prototyping stage. However, its specifications suggest that the component offers superior performance compared to the Avago variant, and it is therefore worth consideration upon manufacturer release.

Next, a mixer is selected. Since the architecture of the imaging does not restrict the design to a specific choice of IF, shown in Chapter 3, there is flexibility in the mixer choice. If desired, the system could be implemented with a zero-IF, or direct conversion to baseband. In this case, both the RF and LO signals would be equal, and the imaging signal would be recovered at DC. In order to resolve magnitude and phase information for complex *S*-parameters, the mixer should then be an I/Q (in-phase/quadrature) type [7][8]. Finding suitable low-noise mixers with conversion gain in the desired frequency band is challenging. For the sake of simplicity, a non-zero IF is used in the prototyping of the system. The Mini-circuits MDA4-752H+ mixer [9] is selected and a manufacturer-provided evaluation board (part number TB-771+ [9]) is used to ensure peak performance. It operates between 2.2 GHz and 7.5 GHz and requires 0 dBm input power at the LO port to achieve 7.3 dB of conversion gain at 6 GHz. It features a 1-dB input compression point of 9 dBm and a noise figure of approximately 10 dB.

5.4. Implementation

For evaluation purposes, the Avago VMMK-3803 is selected. A pair of circuit boards containing the necessary biasing network and PCB transmission lines are designed and fabricated, reported in [10] by Tajik. The board is designed following Avago’s recommendations, using a coplanar waveguide (CPW) structure. Vias connecting the top ground plane to the bottom are placed approximately 1 mm apart along the perimeter of the board and the border of the CPW. FIG. 5-1 shows a photo of the completed prototype.

The performance of the two cascaded prototypes is evaluated with an Agilent E83638 PNA network analyzer [11] and compared with the manufacturer-provided *S*-parameters. FIG. 5-2 shows the input return loss of the prototype and the simulated pair of cascaded LNAs, using Avago’s data. The simulated input return loss is generated in AWR Design Environment 11 [12] using two identical, cascaded subcircuits containing the *S*-parameters of a single LNA, provided by Avago. Note that there is a significant difference between the two data sets. The Avago data are calibrated at the reference plane of the LNA chip itself, whereas the prototype calibration is referenced at the SMA ports used to connect to the VNA. Therefore, this discrepancy in performance may be attributed to the design of the board. Regardless, using the return loss optimization goal of the antenna design as a guide, the dual LNA return loss is still below 5 dB between 6 GHZ and 6.75 GHz and beyond 7.5 GHz, which is sufficient for prototyping purposes.

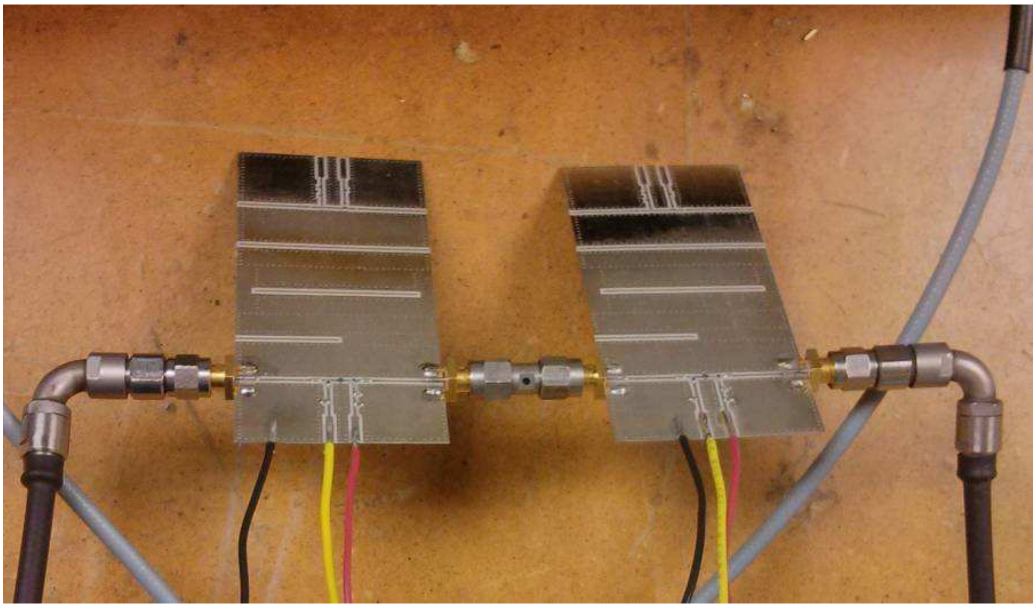

FIG. 5-1. Photo of two cascaded LNAs.

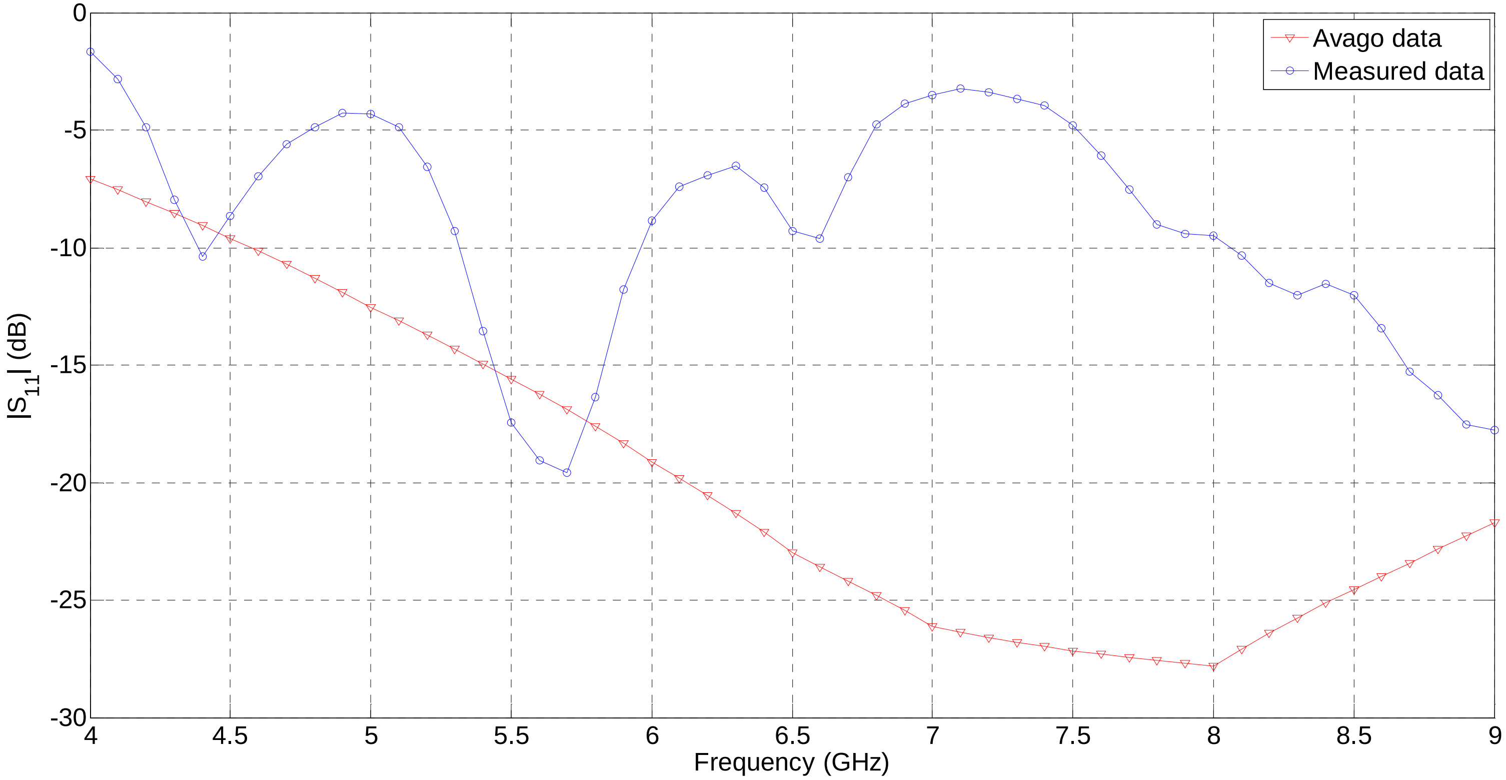

FIG. 5-2. Return loss vs. frequency for manufacturer data and prototype measurements of two cascaded LNAs.

Next, the difference in insertion loss between bias states is measured. When the amplifiers are biased ON and OFF, the insertion loss is measured to quantify the LNA network’s ability to act as a switch. The results are shown in FIG. 5-3. These measurements were performed with an input test power of -30 dBm from the VNA to prevent the possibility of saturation. The data are in closer agreement for insertion loss than for return loss, comparing between the manufacturer data and the prototype measurements. They indicate that approximately 80 dB of difference between ON and OFF bias states in the observed insertion loss is available with the two cascaded LNAs. This is comparable or better than the inter-port isolation available in surface-mount technology microwave switches [13].

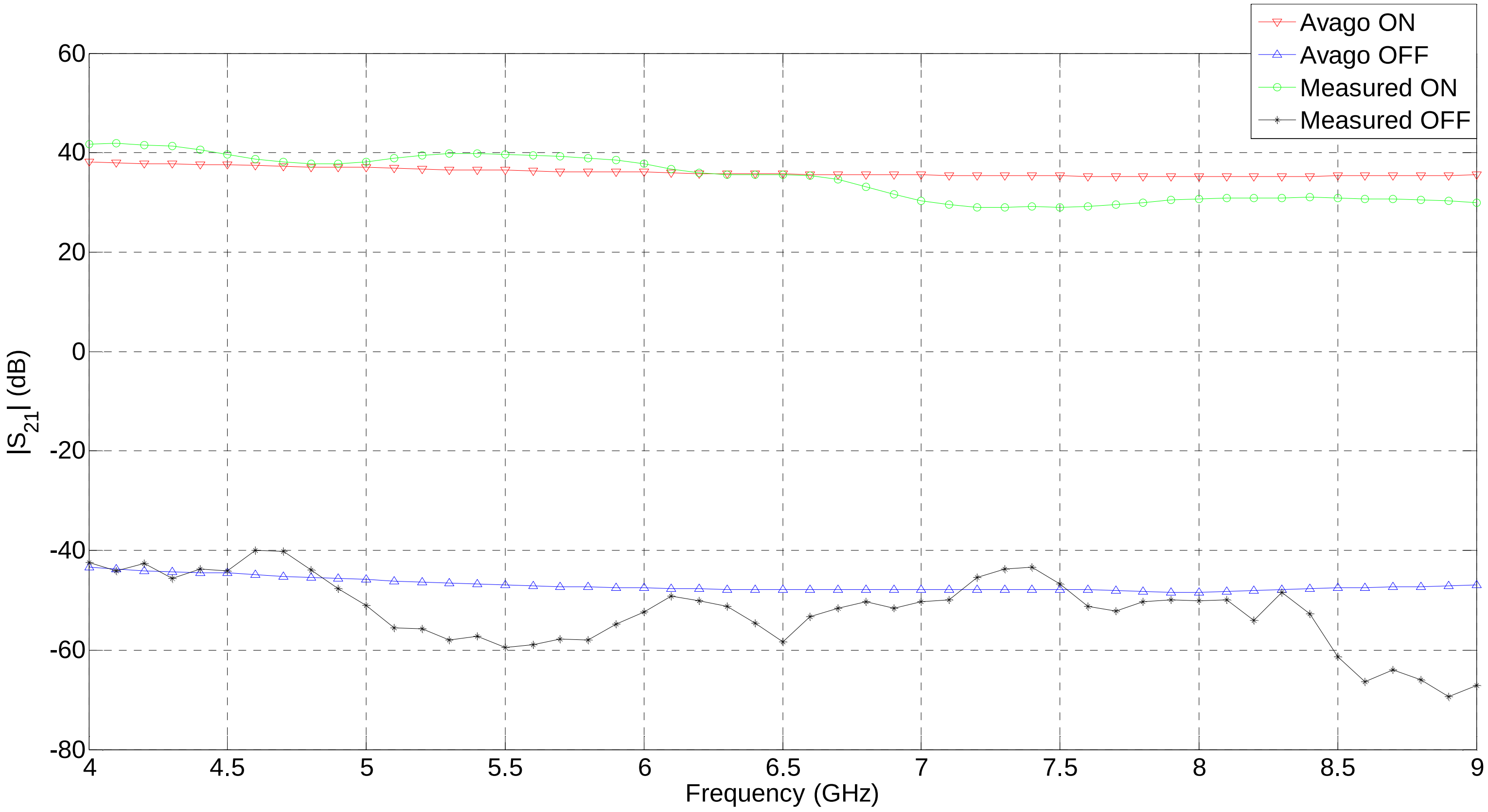

FIG. 5-3. Insertion loss vs frequency; manufacturer (Avago) data and measured data.

After verifying the performance of the LNAs, the mixer is connected following the LNA network and a test is performed to quantify the difference between the full receiver ON state bias and OFF state bias, at the system IF. A system IF of 30 MHz is adopted for the purposes of testing, as this is the lowest manufacturer-recommended frequency that can be used at the Mini-circuits mixer IF port. The Agilent E83638 PNA network analyzer [11] is configured for constant-wave operation with an output power of -40 dBm at a frequency of 6.5 GHz, connected to the input port of the cascaded LNAs. An HP Synthesized CW Generator Model 8671B [14] is used as the source for the mixer LO port, set to 0 dBm output power at a frequency of 6.53 GHz. Measurements of the IF port power are taken using an HP 8593E Spectrum Analyzer [15], with the resolution bandwidth set to 300 Hz. The noise floor of the spectrum analyzer in this configuration is approximately -126 dBm.

Four biasing conditions are evaluated:

State 1: All active devices ON; LNAs: 3 V, mixer: 5 V

State 2: LNAs OFF, mixer ON

State 3: LNAs ON, mixer OFF

State 4: All active devices OFF

The output power at the system IF of 30 MHz for each state is as follows:

State 1: 1.6 dBm

State 2: -86 dBm

State 3: -102 dBm

State 4: -126 dBm (noise floor of instrument reached)

Between the full ON bias condition (State 1) and full OFF bias condition (State 4), there is at least 127 dB of difference in the observed IF power. The remaining bias conditions are evaluated in order to quantify the effect of switching only one device ON and OFF, which may be advantageous in developing a simpler PCB layout containing all radio receiver modules. Regardless, limiting the system bias conditions to State 1 and State 4 achieves the best performance and will save the most power, since only one set of active components will be biased ON at a time in the entire array of switched sensors.

The full system 1-dB compression point is measured using the same configuration described previously in the bias switching experiment. The Agilent PNA output power is increased gradually until the system gain at the IF decreases by 1 dB. This compression point at a test frequency of 6.5 GHz is found to be approximately -36 dBm.

The total noise figure of the 3 cascade active devices is calculated according to the Friis formula [16]:

$$F = F_1 + \frac{F_2 - 1}{G_1} + \frac{F_3 - 1}{G_1 G_2}. \tag{5.1}$$

The values F_n represent the noise factor (non-dB equivalent of noise figure) of the n-th stage in the receiver, with G_n representing the gain of the n-th receiver stage (non-dB scale). Using the manufacturer-provided data, the expected system noise factor is therefore:

$$F = 10^{0.15} + \frac{10^{0.15} - 1}{10^{1.786}} + \frac{10^{1} - 1}{\left(10^{1.786}\right)^{2}} \approx 1.4217\,. \tag{5.2}$$

This noise factor is equivalent to a noise figure of 1.53 dB, a reasonably low value.

In order to calculate the receiver sensitivity, first the minimum detectable signal (MDS) is calculated, following the derivation in [17]:

$$MDS = -174\,\mathrm{dBm} + 10\log B + NF_{\mathrm{sys}} = -174 + 10\log B + 1.53. \tag{5.3}$$

Here, B is the bandwidth of the signal, NF_{sys} is the noise figure of the system. Using an IF bandwidth of 10 kHz, for example, this implies an MDS of:

$$MDS = -174 + 10\log 10000 + 1.53 = -132.47\,\mathrm{dBm}. \tag{5.4}$$

Finally, the sensitivity can be calculated [17] as:

$$Sensitivity = MDS + SNR. \tag{5.5}$$

Assuming a minimum desired SNR of 10 dB:

$$Sensitivity = -132.47 + 10 = -122.47\,\mathrm{dBm}. \tag{5.6}$$

This is the minimum required signal strength to achieve the specified SNR. Together with the 1-dB compression point of the receiver, the dynamic range of the whole system [17] is:

$$\begin{aligned} DR &= CP_{1dBin} - MDS_{dBm} \\ &= -36 - \left(-132.47\right) \\ &= 96.47\,\mathrm{dB}. \end{aligned} \tag{5.7}$$

This dynamic range is comparable with the SNR of a 16-bit ADC (Eq. 3.1). The dynamic range can be improved in the hardware by choosing a lower IF. This is because lower IF allows for using more narrowband filters, which in turn means lower noise levels. For instance, reducing the IF bandwidth to 1 kHz increases the dynamic range to 106.47 dB, 10 dB greater than the previous estimate. The imaging system dynamic range can be improved further with averaging, as is demonstrated in [18].

5.5. Conclusions

The design of a miniature radio front-end is presented for use in a switched sensor microwave imaging system. Components are chosen based on the figures-of-merit listed in Chapter 2 and an experimental prototype is constructed for measurements. The prototype achieves significant separation in IF power of approximately 127 dB between two bias states and can therefore be used directly in an imaging array without including additional RF switches. Estimates are made for the sensitivity and suggest that the system can have a dynamic range approaching 110 dB with sufficiently narrow IF filtering.

REFERENCES

[1] M. Klemm, J.A. Leendertz, D. Gibbins, I.J. Craddock, A. Preece, and R. Benjamin, “Microwave radar-based differential breast cancer imaging: imaging in homogeneous breast phantoms and low contrast scenarios,” *IEEE Trans. Antennas Propagat.*, vol. 58, no. 7, pp. 2337–2344, Jul. 2010.

[2] P.M. Meaney, M.W. Fanning, D. Li, S.P. Poplack, and K.D. Paulsen, “A clinical prototype for active microwave imaging of the breast,” *IEEE Trans. Microwave Theory and Techniques*, vol. 48, no. 11, pp. 1841−1853, Nov. 2000.

[3] M.E. Bialkowski, A.M. Abbosh, Y. Wang, D. Ireland, A.A. Bakar, and B.J. Mohammed, “Microwave imaging systems employing cylindrical, hemispherical and planar arrays of ultrawideband antennas,” *2011 Asia-Pacific Microwave Conf. Proc. (APMC)*, pp. 191−194, Dec. 2011.

[4] Hewlett-Packard, “IAM-8 series active mixers application note S013”, [Online]. Available: http://www.hp.woodshot.com/hprfhelp/4_downld/lit/iclit/ans013.pdf

[5] Avago VMMK-3803 3-11 GHz UWB Low Noise Amplifier in WaferCap SMT Package, http://www.avagotech.com /products/wireless/amplifiers/ low-noise/vmmk-3803

[6] Mini-circuits PMA3-83LN+ Monolithic Amplifier 0.5 to 8.0 GHz, http://www.minicircuits.com (available upon request)

[7] A. Mashhour, W. Domino, and N. Beamish, “On the direct-conversion receiver – a tutorial,” *Microwave Journal* [Online]. Available: http://www.microwavejournal.com/articles/3226-on-the-direct-conversion-receiver-a-tutorial

[8] B. Razavi, “Design considerations for direct-conversion receivers”, *IEEE Trans. Circuits and Systems II: Analog and Digital Signal Processing*, vol. 44, no. 6, pp. 428−435, Jun. 1997.

[9] Mini-circuits MDA4-752H+ Wideband Double Balanced Mixer-Amplifier, http://www.minicircuits.com/pdfs/MDA4-752H+.pdf

[10] D. Tajik, “S-parameter quantification of a VMMK-3803 low noise Amplifier for microwave imaging,” *McMaster 4OJ4 Technical Report,* Dec. 2014

[11] Agilent E83638 PNA network analyzer

[12] NI AWR Design Environment, Version 11.02r build 7015, AWR – A National Instruments Company, 2014.

[13] P. Hindle, “The state of RF and microwave switches,” *Microwave Journal* [Online]. Available: http://www.microwavejournal.com/articles/10269-the-state-of-rf-and-microwave-switches

[14] HP Synthesized CW Generator Model 8671B

[15] HP 8593E Spectrum Analyzer

[16] D.M. Pozar, *Microwave Engineering*. 4th ed., Hoboken: John Wiley & Sons, Inc., 2012.

[17] M. Loy, “Understanding and enhancing sensitivity in receivers for wireless applications,” *Texas Instruments Technical Brief SWRA030* [Online]. Available: www.ti.com/lit/an/swra030/swra030.pdf

[18] B. Brown and J. Bains, “Improving the vector network analyzer’s dynamic range,” *RF Design* [Online]. Available: http://images.rfdesign.com/files/4/0900Brown82.pdf

CHAPTER 6

EXPERIMENTAL VERIFICATION

6.1. Hardware Testing in an Imaging Scenario

In order to evaluate the antenna and LNA performance in a realistic imaging environment, the prototype array and amplifier networks are connected to a commercial VNA for testing. A raster scan imaging system has been constructed for the purpose of acquiring data from breast phantoms:

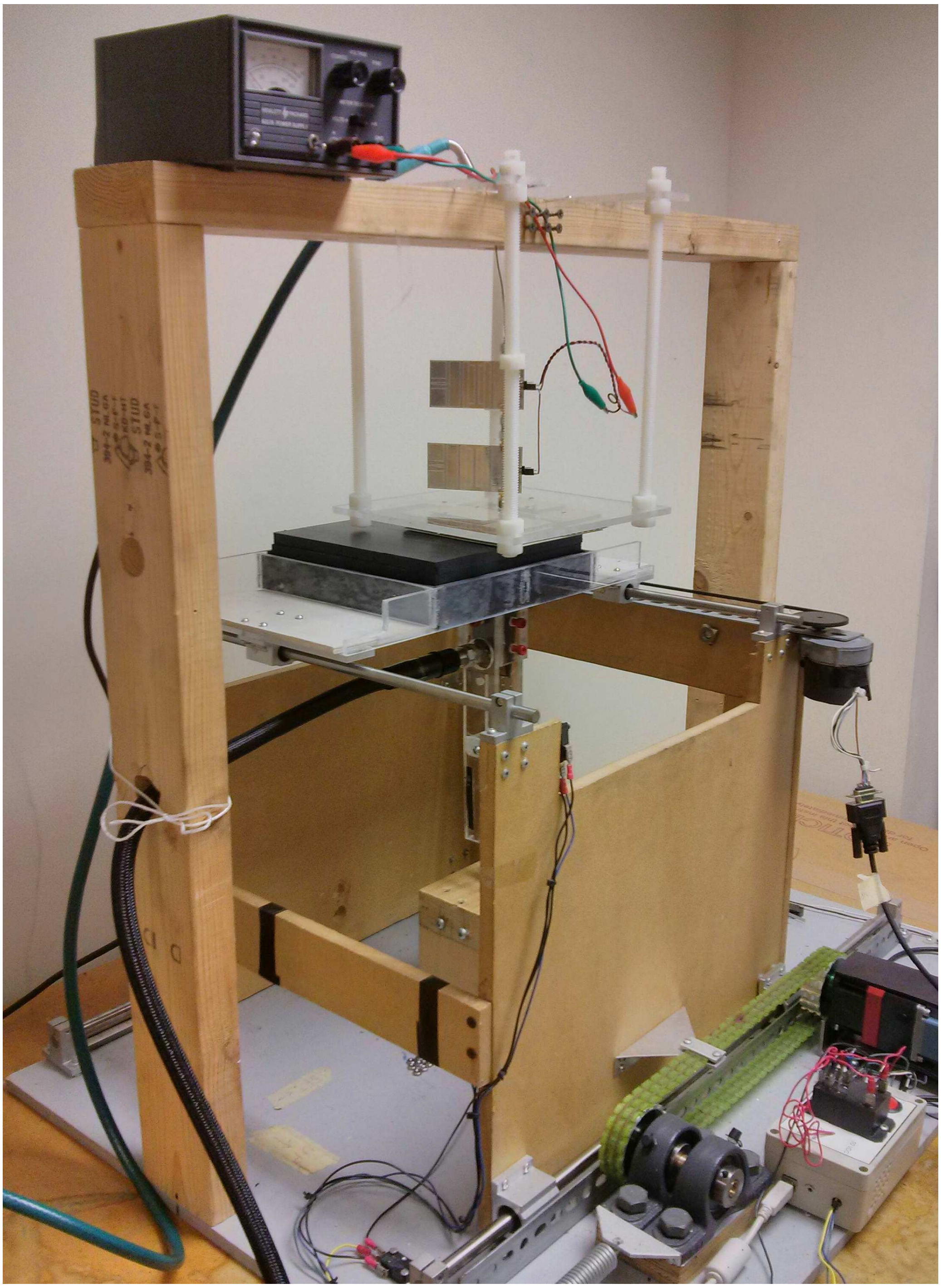

FIG. 6-1. Photograph of *x*-*y* scanner with 5-layer phantom, TEM horn, antenna array, and LNA network.

The horn antenna described by Reza in [1] is used as the OUT illumination source. The fabricated 3x3 antenna array prototype is located opposite this antenna, displaced by a stack of 5 Emerson & Cuming absorbing sheets, described in the previous chapters as an imaging phantom. In the second absorber sheet layer down from the top, a single 1 cm diameter, 1 cm deep hole is cut-out in the centre. Embedded in this cut-out is a dielectric cylinder with $\varepsilon_r = 50$ and $\tan\delta \approx 0.001$, serving as a tumor phantom, whose electrical properties contrast strongly with the neighbouring medium:

FIG. 6-2. Phantom layer with embedded dielectric cylinder.

The array prototype is configured only to use the central antenna element for the purposes of testing. Thus, full mechanical translation of the phantom is necessary to achieve adequate spatial sampling. Planar raster scanning is performed over an area of 100 mm x 100 mm in 2 mm steps using the computer-controlled *x-y* scanner. An Advantest R3770 Network Analyzer [2] is used for data acquisition. For every coordinate position, the computer triggers the VNA to perform *S*-parameter measurements over a frequency band of 3 GHz to 10 GHz in 0.1 GHz steps (71 points). A resolution bandwidth of 10 kHz is used. The VNA output power, fed to the terminals of the TEM horn, is set to 8 dBm. Four data averages are taken per measurement, and smoothing is applied over an aperture of 16%. The VNA acquires the complex *S*-parameter S_{21}, measuring the transmission coefficient from the horn antenna to the centre element of the 3x3 prototype array. LNA bias is supplied externally with a single DC power supply set to 3 V.

FIG. 6-3 contains an image of the raw data component $10\log|S_{21}|$, measured at 6.7 GHz, generated with MATLAB [3]. Notice that the dielectric cylinder is clearly discernable in this qualitative image:

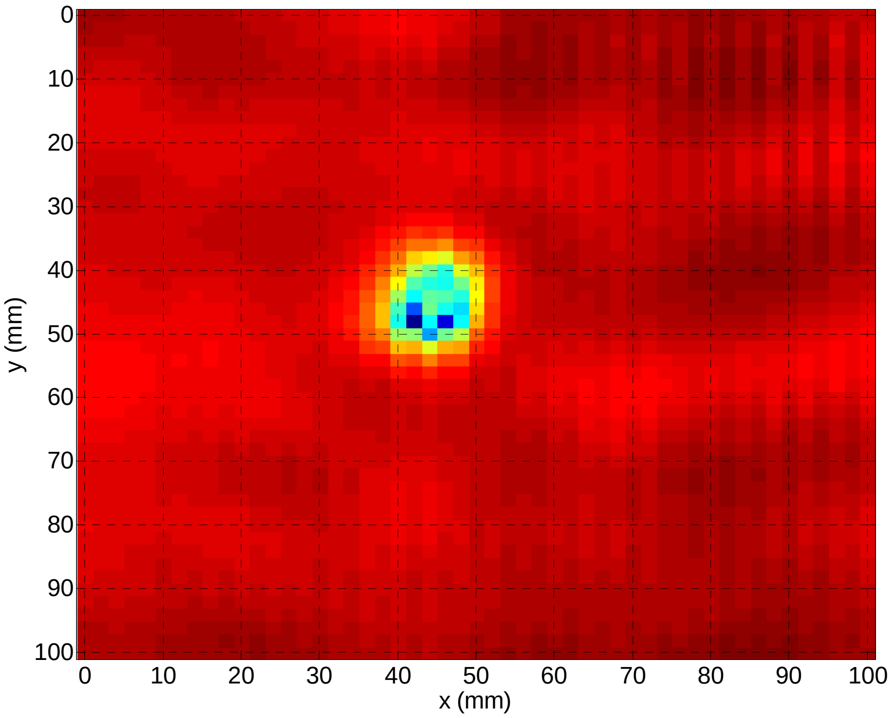

FIG. 6-3. Log-magnitude raw measurement data of phantom at 6.7 GHz.

In order to quantify the performance of the system as configured, a method for calculating the image SNR described by McCombe in [4] is used. A second image of the same phantom is taken, replacing the high permittivity dielectric cylinder with absorber sheet material. This data is used in the SNR algorithm to calibrate the system, removing *S*-parameter errors collected in measuring transmission through the background medium. An algorithm developed in MATLAB is used to perform the SNR calculations, shown in the following figure:

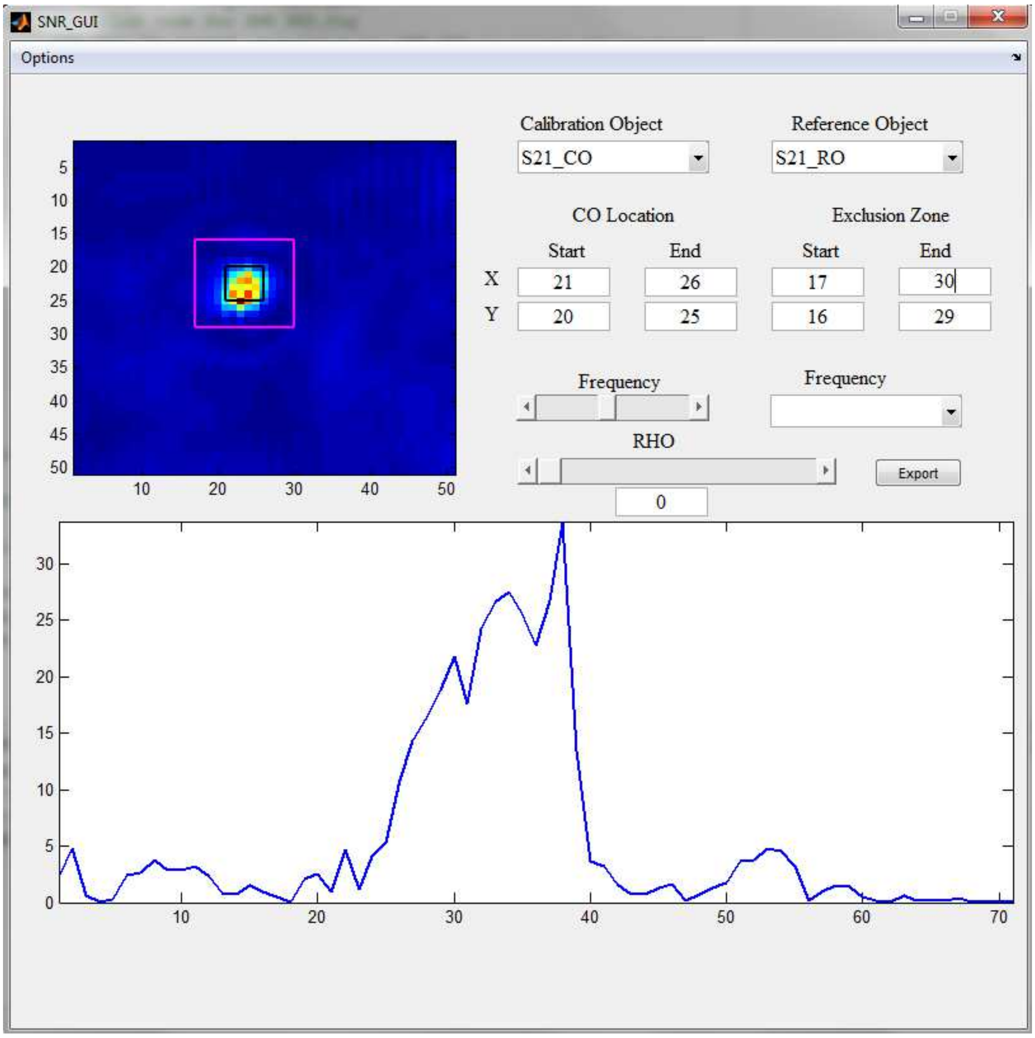

Calibration Object: S21_CO

Reference Object: S21_RO

	CO Location Start	CO Location End	Exclusion Zone Start	Exclusion Zone End
X	21	26	17	30
Y	20	25	16	29

RHO: 0

FIG. 6-4. Image SNR calculation MATLAB applet.

This applet’s calculations suggest that the best log-magnitude raw data SNR available with the antenna and LNAs connected to the VNA is approximately 30, nearly 15 dB, at a frequency of 6.7 GHz (frequency point 37 of 71). The performance is expected to be highest in this range since the antenna structure is optimized for operation close to this frequency. This performance is comparable with previously reported results in [5] using the same *x*-*y* scanner and TEM horn, and an array of RF-switched bow tie antennas as receiving elements.

6.2. Conclusions

An experimental image acquisition is performed with the prototype antenna element and LNA modules using an *x*-*y* scanner and a commercial VNA. Results demonstrate that the antenna and amplifier components of the proposed imaging system operate as specified in the design.

REFERENCES

[1] R.K. Amineh, A. Trehan, and N.K. Nikolova, “TEM horn antenna for ultra-wide band microwave breast imaging,” *Progress In EM Research B (PIER B)*, vol. 13, pp. 59−74, 2009.

[2] Advantest R3770 Network Analyzer

[3] MATLAB 2012b

[4] J.J. McCombe and N.K. Nikolova, “SNR assessment of microwave imaging systems,” *IEEE AP-S/URSI Int. Symp. Antennas and Propagat.*, Jul. 2014.

[5] S. Tu, J.J. McCombe, and N.K. Nikolova, “Fast quantitative microwave imaging with resolvent kernel extracted from measurements,” *Inverse Problems* (major revision submitted Nov. 21, 2014)

CHAPTER 7

CONCLUSION AND FUTURE WORK

7.1. Imaging System Design Conclusions

In Chapter 1, a general outline of microwave imaging was given with focus on medical applications in breast cancer screening. Current advances in the state-of-the-art were discussed in the context of the various technical challenges involved in tissue imaging. Chapter 2 elaborated on these technical challenges, providing a list of valuable figures-of-merit used to assess the performance of imaging systems. In the following chapter, a novel imaging architecture was proposed, aiming to overcome the performance limits reported in the literature. The proposed architecture consists of an electronically-switched array of sensors with integrated radio receivers and a wireless local oscillator signal path. Image acquisition is accomplished with a VNA-based *S*-parameter measurement module.

The complete imaging system was described in 3 parts: the signal path and signal processing hardware were examined first in Chapter 3; the imaging sensor, consisting of an antenna and radio front-end, was described in Chapters 4 and 5.

A prototype of the imaging sensor was constructed and tested in the lab, comparing experimental data with the results predicted by the manufacturers' specifications. It achieves a sensor insertion loss dynamic range between ON and OFF states of at least 127 dB, exceeding the performance of conventional RF switches while integrating a sensitive heterodyne receiver in a small form-factor. This prototype was then evaluated with experimental imaging measurements in Chapter 6, demonstrating the design's feasibility.

7.2. Future Work

Preliminary results generated with mechanical scanning of the prototype suggest that the design is realizable using inexpensive fabrication methods and components. However, only one antenna has been used in these measurements. It is not yet certain what the image fidelity will be when a large array of closely spaced antenna elements is implemented. Since the current imaging phantoms used in the previous experiments are 20 cm by 20 cm in size, an array of at least 100 sensors (10x10) should be fabricated. This would provide an acquisition surface area of at least 13.5 cm by 13.5 cm before adding mechanical scanning. It is anticipated that the measurement time can be dramatically reduced in the final array-based system, replacing full mechanical scanning of the phantom with a combination of partial scanning and electronic array switching. This will improve the feasibility of implementing such a system in a medical diagnostic environment, where a large patient roster is expected on an annual basis.

As the primary application of this switched transceiver design is in medical imaging, it is critical to understand how the system influences the temperature of the imaged tissues. Thus, a study of the specific absorption rate (SAR) and the heating of tissues will be necessary before pursuing any medical trials.

More rigorous optimization may be applied to the antenna structure and the array in an effort to improve the total system performance. A study of the antenna design's sensitivity with respect to shape parameters could also yield important results about the machining tolerances necessary when manufacturing a final design. An investigation on the inclusion of a superstrate, adding an additional layer of tissue-matching dielectric above the patch antennas, may prove yet more valuable in mitigating the design's sensitivity to the presence of the rather heterogeneous volume of tissues involved in breast imaging.

A complete signal path, including all components of the VNA-based *S*-parameter measurement system, should be constructed in order to assess the limits in detector sensitivity in a real imaging scenario. The proposed architecture is sufficiently modularized and broad in its description that a variety of signal sources and digitization hardware could be explored, optimizing each subsection independently. Effort should be made to exceed the performance attained using commercially-available equipment while minimizing complexity and cost in the hardware design.

The above single-channel acquisition should be extended to a multiple-channel system, initially aiming at five to six signal paths. Such a system would be beneficial in a planar rotating scenario where spiral arrangements of the antenna arrays are used. The existing facilities include a precision rotating scanner and, therefore, provide the opportunity to test and improve such a system.

Finally, the large array of at least 100 sensors (10x10) should be fabricated. This implies at least 100 signal paths. This system is to be used in electronically switched planar scanning of tissues.

Beyond these areas of research, it would be beneficial to consider imaging on surfaces that better accommodate the geometry of typical breasts. Thus, the design of cylindrical and hemispherical imaging arrays should be explored. Another implementation could involve the design of wearable electronics; manufacturing a wearable system that collected data about a patient’s breasts over time could provide a consistent stream of diagnostic information to doctors, thereby improving the likelihood of cancer detection.

BIBLIOGRAPHY

A. Chenakin, “Select a VCO or YIG for a PLL synthesizer?” [Online]. Available: http://mwrf.com/active-components/select-vco-or-yig-pll-synthesizer

A. Hati, C.W. Nelson, D.A. Howe, N. Ashby, J. Taylor, K.M. Hudek, C. Hay, D. Seidef, and D. Eliyahu, “Vibration sensitivity of microwave components,” *2007 Joint 21st European Freq. Time Frm. IEEE Int. Freq. Control Symp.*, pp. 541–546, May 29–June 1, 2007.

A. Mashhour, W. Domino, and N. Beamish, “On the direct-conversion receiver – a tutorial,” *Microwave Journal* [Online]. Available: http://www.microwavejournal.com/articles/3226-on-the-direct-conversion-receiver-a-tutorial

A.S. Beaverstone and N.K. Nikolova, “Modeling and design of a switched transceiver array for tissue imaging,” *IEEE MTT-S Int. Conf. Num. EM and Multiphys. Modeling and Opt. 2015*, Aug. 2015.

A.S. Beaverstone and N.K. Nikolova, “Switched sensor array for near-field microwave imaging of tissue,” *IEEE Int. Symp. Antennas Propagat. North American Radio Science Meeting*, no. 4765, Jul. 2015.

Advantest R3770 Network Analyzer

Agilent E83638 PNA network analyzer

Analog Devices AD8302 RF/IF Gain and Phase Detector, LF-2.7 GHz, http://www.analog.com/media/en/technical-documentation/evaluation-documentation/AD8302.pdf

Analog Devices AD8307 Logarithmic Amplifier, DC to 500 MHz, http://www.analog.com/media/en/technical-documentation/data-sheets/AD8307.pdf

ANSYS HFSS, Version 15.0.2, ANSYS Inc., Southpointe, 2600 ANSYS Drive, Canonsburg, PA 15317, 2013.

Avago VMMK-3803 3-11 GHz UWB Low Noise Amplifier in WaferCap SMT Package, http://www.avagotech.com /products/wireless/amplifiers/ low-noise/vmmk-3803

B. Brown and J. Bains, “Improving the vector network analyzer’s dynamic range,” *RF Design* [Online]. Available: http://images.rfdesign.com/files/4/0900Brown82.pdf

B. Razavi, “Design considerations for direct-conversion receivers”, *IEEE Trans. Circuits and Systems II: Analog and Digital Signal Processing*, vol. 44, no. 6, pp. 428−435, Jun. 1997.

B.C. Henderson and J.A. Cook, “Image-reject and single-sideband mixers,” WJ Communications Inc., [Online]. Available: http://www.rfcafe.com/references/articles/wj-tech-notes/ImageRej_n_SSB_mixers.pdf

C.A. Balanis, *Antenna Theory: Analysis and Design.* 3rd ed. Hoboken, NJ: John Wiley & Sons Inc., 2005.

D. Andreuccetti, R. Fossi, and C. Petrucci, “An Internet resource for the calculation of the dielectric properties of body tissues in the frequency range 10 Hz - 100 GHz,” (IFAC-CNR), [Online] 1997, http://niremf.ifac.cnr.it/tissprop (Accessed May 2015).

D. Faktorová, “Temperature dependence of biological tissues complex permittivity at microwave frequencies,” *Adv. in Electrical and Electronic Eng.*, vol. 7, pp. 354–357, 2008.

D. Tajik, “S-parameter quantification of a VMMK-3803 low noise Amplifier for microwave imaging,” *McMaster 4OJ4 Technical Report*, Dec. 2014

D.M. Pozar, *Microwave Engineering*. 4th ed., Hoboken: John Wiley & Sons, Inc., 2012.

H. Schantz, *The Art and Science of Ultra-Wideband Antennas.* Norwood: Artech House Inc., 2005.

Hewlett-Packard, “IAM-8 series active mixers application note S013”, [Online]. Available: http://www.hp.woodshot.com/hprfhelp/4_downld/lit/iclit/ans013.pdf

HP 8593E Spectrum Analyzer

HP Synthesized CW Generator Model 8671B

J. Bourqui, J. M. Sill, and E. C. Fear, “A prototype system for measuring microwave frequency reflections from the breast,” *Int. Journal of Biomedical Imaging*, vol. 2012, Article ID 851234, 12 pages, 2012.

J.-C. Bolomey and F.E. Gardiol, *Engineering Applications of the Modulated Scatterer Technique*. Norwood, MA: Artech, 2001.

J.-C. Bolomey, “Technology-based analysis of probe array systems for rapid near-field imagery and dosimetry,” *2014 8th European Conf. Antennas and Propagat. (EuCAP)*, pp. 3115−3119, April 2014.

J.C. Lin, “Frequency optimization for microwave imaging of biological tissues,” *IEEE Proc.*, vol. 73, no. 2, pp. 374–375, Feb. 1985.

J.J. McCombe and N.K. Nikolova, “SNR assessment of microwave imaging systems,” *IEEE AP-S/URSI Int. Symp. Antennas and Propagat.*, Jul. 2014.

J.R. Thompson, J.J. McCombe, S. Tu, and N.K. Nikolova, “Quantitative imaging of dielectric objects based on holographic reconstruction,” 2015 *IEEE Int. Radar Conf.*, Arlington, VA.

K.C. Gupta and A. Benalla, *Microstrip Antenna Design*. Norwood: Artech House, 1988.

Keysight Technologies PNA Network Analyzer, 300 kHz to 1.1 THz, http://www.keysight.com/en/pc-1000001745%3Aepsg%3Apgr/pna-network-analyzers-300-khz-to-11-thz?cc=CA&lc=eng

Keysight Technologies, “Understanding and improving network analyzer dynamic range, application note,” [Online]. Available: cp.literature.agilent.com/litweb/pdf/5980-2778EN.pdf

L.E. Larsen and J.H. Jacobi, “Microwave interrogation of dielectric targets. Part I: By scattering parameters,” *Med. Phys.*, vol. 5, no. 6, 1978, pp. 500–508.

L.E. Larsen and J.H. Jacobi, “Microwave interrogation of dielectric targets. Part II: By microwave time delay spectroscopy,” *Med. Phys.*, vol. 5, no. 6, 1978, pp. 509–513.

L.E. Larsen and J.H. Jacobi, “The Use of Orthogonal Polarizations in Microwave Imagery of Isolated Canine Kidney,” *IEEE Trans. Nuclear Science*, vol. 27, no. 3, pp. 1183–1191, June 1980.

L.E. Larsen and J.H. Jacobi, eds., *Medical Applications of Microwave Imaging*. New York: IEEE Press, 1986.

M. Hiebel, *Fundamentals of Vector Analysis*. 1st ed., München: Rohde & Schwartz GmbH & Co. KG, 2007.

M. Klemm, J.A. Leendertz, D. Gibbins, I.J. Craddock, A. Preece, and R. Benjamin, “Microwave radar-based differential breast cancer imaging: imaging in homogeneous breast phantoms and low contrast scenarios,” *IEEE Trans. Antennas Propagat.*, vol. 58, no. 7, pp. 2337–2344, Jul. 2010.

M. Loy, “Understanding and enhancing sensitivity in receivers for wireless applications,” *Texas Instruments Technical Brief SWRA030* [Online]. Available: www.ti.com/lit/an/swra030/swra030.pdf

M. Pastorino, *Microwave Imaging*. Hoboken, NJ: John Wiley & Sons Inc., 2010.

M. Ravan, R.K. Amineh, and N.K. Nikolova, “Two-dimensional near-field microwave holography,” *Inverse Problems*, vol. 26, No. 5, 055011, May 2010.

M.E. Bialkowski, A.M. Abbosh, Y. Wang, D. Ireland, A.A. Bakar, and B.J. Mohammed, “Microwave imaging systems employing cylindrical, hemispherical and planar arrays of ultrawideband antennas,” *Microwave Conf. Proc. (APMC), 2011 Asia-Pacific*, pp. 191−194, Dec. 2011.

M.E. Bialkowski, A.M. Abbosh, Y. Wang, D. Ireland, A.A. Bakar, and B.J. Mohammed, “Microwave imaging systems employing cylindrical, hemispherical and planar arrays of ultrawideband antennas,” *2011 Asia-Pacific Microwave Conf. Proc. (APMC)*, pp. 191−194, Dec. 2011.

MATLAB 2012b

Mini-circuits MDA4-752H+ Wideband Double Balanced Mixer-Amplifier, http://www.minicircuits.com/pdfs/MDA4-752H+.pdf

Mini-circuits PMA3-83LN+ Monolithic Amplifier 0.5 to 8.0 GHz, http://www.minicircuits.com (available upon request)

N. Kuga and H. Arai, “Circular Patch Antennas Miniaturized by Shorting Posts,” *Electron. Comm. Japan (part I: Communications)*, vol. 79, no. 6, pp. 51–58, Oct. 1996. [Online]. Available: http://onlinelibrary.wiley.com/doi/10.1002/ecja.4410790606/pdf. (Accessed Jan. 8, 2015).

N.K. Nikolova, “Microwave biomedical imaging,” *Wiley Encyclopedia of Electrical and Electronics Engineering*, pp. 1–22. (published on-line Apr. 25, 2014).

National Instruments, “1 dB gain compression measurement (P1dB)”, [Online]. Available: http://www.ni.com/white-paper/2952/en/

National Instruments, “Super-heterodyne signal analyzers description and applications,” [Online]. Available: http://download.ni.com/evaluation/rf/Super_Heterodyne_Signal_Analyzers.pdf

NI AWR Design Environment, Version 11.02r build 7015, AWR – A National Instruments Company, 2014.

P. Hindle, “The state of RF and microwave switches,” *Microwave Journal* [Online]. Available: http://www.microwavejournal.com/articles/10269-the-state-of-rf-and-microwave-switches

P. Kumar and G. Singh, “Microstrip antennas loaded with shorting post,” *Engineering* 1(1), pp. 41–45, 2009.

P.M. Meaney, M.W. Fanning, D. Li, S.P. Poplack, and K.D. Paulsen, “A clinical prototype for active microwave imaging of the breast,” *IEEE Trans. Microwave Theory and Techniques*, vol. 48, no. 11, pp. 1841−1853, Nov. 2000.

R. K. Amineh, M. Ravan, A. Khalatpour, and N.K. Nikolova, “Three-dimensional near-field microwave holography using reflected and transmitted signals,” *IEEE Trans. Antennas Propagat.*, vol. 59, no. 12, pp. 4777–4789, Dec. 2011.

R. Waterhouse, S.D. Targonski, and D.M. Kokotoff, “Design and Performance of Small Printed Antennas,” *IEEE Trans. Antennas Propagat.*, vol. 46, no. 11, pp. 1629–1633, Nov. 1998. [Online]. Available: http://ieeexplore.ieee.org/stamp/stamp.jsp?arnumber=736612. (Accessed Jan. 8, 2015).

R.K. Amineh, A. Trehan, and N.K. Nikolova, “TEM horn antenna for ultra-wide band microwave breast imaging,” *Progress In EM Research B (PIER B)*, vol. 13, pp. 59−74, 2009.

R.K. Amineh, M. Ravan, A. Trehan, and N.K. Nikolova, “Near-field microwave imaging based on aperture raster scanning with TEM horn antennas,” *IEEE Trans. Antennas Propagat.*, vol. 59, no. 3, pp. 928–940, Mar. 2011.

Rogers RT/duroid ® 6006/6010LM High Frequency Laminates, http://www.rogerscorp.com/documents/612/acs/RT-duroid-6006-6010LM-laminate-data-sheet.pdf

S. Tu, J.J. McCombe, and N.K. Nikolova, “Fast quantitative microwave imaging with resolvent kernel extracted from measurements,” *Inverse Problems* (major revision submitted Nov. 21, 2014)

S. Tu, J.J. McCombe, D.S. Shumakov, and N.K. Nikolova. “Fast quantitative microwave imaging with resolvent kernel extracted from measurements,” *Inverse Problems,* vol. 31, no. 4, 2015, 045007.

Skyworks SMP1320-079LF PIN Diode,
http://www.skyworksinc.com/uploads/documents/SMP1320_Series_200047P.pdf

T. Gunnarsson, “Microwave imaging of biological tissues: applied toward breast tumor detection,” Licentiate thesis, Dept. of Comp. Sci. and Electronics, Mälardalen Univ., Västerås, Sweden, 2007.

T.S. Curry, J.E. Dowdey, and R.C. Murry, *Christensen's Physics of Diagnostic Radiology*. 4th ed., Philadelphia: Lippincott Williams & Wilkins, 1990.

W. Kester, “Taking the mystery out of the infamous formula, SNR = 6.02N + 1.76dB, and why you should care,” Analog Devices, [Online]. Available: http://www.analog.com/media/en/training-seminars/tutorials/ MT-001.pdf

Y. Baskharoun, A. Trehan, N.K. Nikolova, and M.D. Noseworthy, “Physical phantoms for microwave imaging of the breast,” *2012 IEEE Topical Conf. Biomedical Wireless Technologies, Networks, and Sensing Systems (BioWireleSS)*, pp. 73–76, Jan. 15–18 2012.